The Influence of Convectively Generated Thermal Forcing on the Mesoscale Circulation around Squall Lines

RAJUL E. PANDYA AND DALE R. DURRAN

Department of Atmospheric Sciences, University of Washington, Seattle, Washington

(Manuscript received 1 December 1995, in final form 15 April 1996)

ABSTRACT

The dynamical processes that determine the kinematic and thermodynamic structure of the mesoscale region around 2D squall lines are examined using a series of numerical simulations. The features that develop in a realistic reference simulation of a squall line with trailing stratiform precipitation are compared to the features generated by a steady thermal forcing in a "dry" simulation with no microphysical parameterization. The thermal forcing in the dry simulation is a scaled and smoothed time average of the latent heat released and absorbed in and near the leading convective line in the reference simulation. The mesoscale circulation in the dry simulation resembles the mesoscale circulation in the reference simulation and around real squall lines; it includes an ascending front-to-rear flow, a midlevel rear inflow, a mesoscale up- and downdraft, an upper-level rear-to-front flow ahead of the thermal forcing, and an upper-level cold anomaly to the rear of the thermal forcing. It is also shown that a steady thermal forcing with a magnitude characteristic of real squall lines can produce a cellular vertical velocity field as the result of the nonlinear governing dynamics. An additional dry simulation using a more horizontally compact thermal forcing demonstrates that the time-mean thermal forcing from the convective leading line alone can generate a mesoscale circulation that resembles the circulation in the reference simulation and around real squall lines.

The ability of this steady thermal forcing to generate the mesoscale circulation accompanying squall lines suggests that this circulation is the result of gravity waves forced primarily by the low-frequency components of the latent heating and cooling in the leading line. The gravity waves in the dry and reference simulation produce a perturbed flow that advects diabatically lifted air from the leading line outward. In the reference simulation, this leads to the development of leading and trailing anvils, while in the dry simulation this produces a pattern of vertically displaced air that is similar to the distribution of cloud in the reference simulation. Additional numerical simulations, in which either the thermal forcing or large-scale environmental conditions were varied, reveal that the circulation generated by the thermal forcing shows a greater sensitivity to variations in the thermal forcing than to variations in the large-scale environment. Finally, it is demonstrated that the depth of the thermal forcing in the leading convective line, not the height of the tropopause, is the primary factor determining the height of the trailing anvil cloud.

1. Introduction

The squall line with trailing stratiform precipitation is one of the most extensively studied types of mesoscale convective systems. As the name implies, this system can be divided into two principal components: 1) a meso-γ-scale leading line of vigorous convection, which produces a strong cellular radar signature and heavy showers, and 2) a meso-β-scale trailing stratiform anvil cloud with much lower reflectivity and weaker, steadier rain. In many of these systems a smaller upper-level stratiform cloud region also extends ahead of the leading line. The contribution of the stratiform rain to the total rainfall is between 40% and 50% (Houze 1977; Gamache and Houze 1985). A schematic diagram of the circulation and cloud structure in a vertical cross section of a prototypical squall line with a trailing stratiform anvil is shown in Fig. 1 (Houze et al. 1989). Two radar reflectivity cells, labeled "mature cell" and "old cell," are shown within the leading line in this schematic diagram. The circulation features indicated in the stratiform region of Fig. 1 are the "ascending front-to-rear flow" and the "descending rear inflow." Buoyancy plays different dynamical roles in the convective and stratiform region of the leading line–trailing anvil system. Within the convective region, buoyancy acts primarily as a destabilizing force; the convective updrafts and downdrafts that constitute the reflectivity cells are positively and negatively buoyant plumes that develop in response to the internal release and absorption of latent heat. In the stratiform region, buoyancy acts primarily as a restoring force allowing the propagation of gravity waves generated by the latent heat released and absorbed in

Corresponding author address: Dr. Rajul Pandya, Department of Atmospheric Sciences, University of Washington, Box 351640, Seattle, WA 98195-1640.
E-mail: pandya@atmos.washington.edu

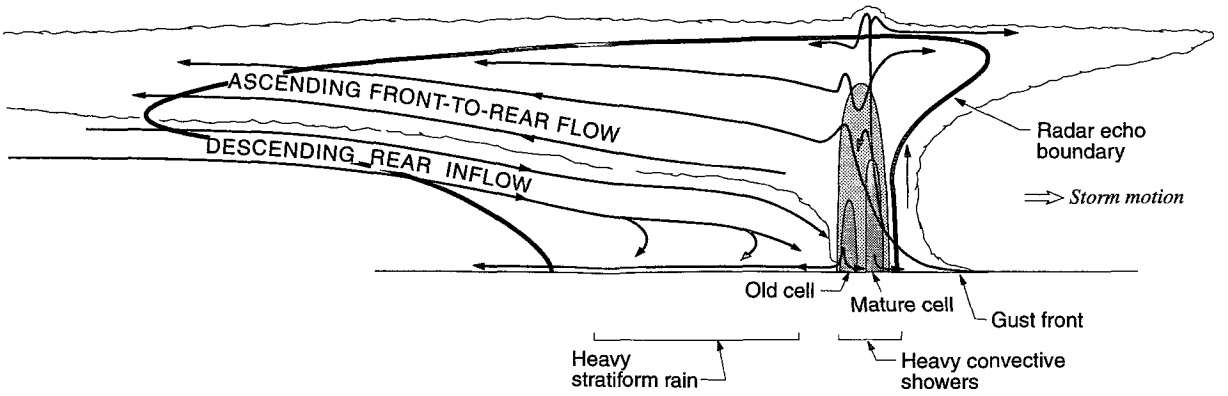

FIG. 1. Conceptual model of a multicell squall line with trailing stratiform precipitation. The storm is viewed in a cross section perpendicular to the convective line (adapted from Houze et al. 1989).

the region of active convection. The thesis of this paper is that the principle kinematic and thermodynamic features of the mesoscale region around squall lines, including the ascending front to rear flow and the descending rear inflow in the trailing anvil, are the result of these gravity waves. An important distinction between the dynamics of the plumes in the convective region and the gravity waves in the stratiform region involves the role of air parcel advection. Plumes propagate primarily through the physical transport of air parcels, whereas small-amplitude gravity waves can propagate without producing any net displacement of air parcels.

Observations have shown that deep convection can generate gravity waves (Miller and Sanders 1980). Conversely, gravity waves have also been implicated in triggering deep convection (Uccellini 1975; Ley and Peltier 1978; Koch et al. 1988). Less well understood is the extent to which deep convection and gravity waves can coexist and mutually interact in order to strengthen and organize mesoscale convective systems. A number of theoretical studies have attempted to elucidate the possible feedbacks between linear gravity waves and convection through analytic or semianalytic wave–CISK formulations in which the thermal forcing from latent heating and cooling is parameterized as a function of the wave-induced flow perturbations (Lindzen 1974; Raymond 1976, 1984; Davies 1979; Xu and Clark 1984; Nehrkorn 1986). Attempts have also been made to identify and interpret the influence of gravity waves in numerical simulations of two-dimensional squall lines (Schmidt and Cotton 1990; Cram et al. 1992; Yang and Houze 1995a). Much of this previous work has been directed toward isolating individual gravity wave modes that play a crucial role in the convection. In the case of wave-CISK, considerable efforts have been devoted to developing heating parameterizations and choosing basic-state environmental profiles that yield a spatial scale for the most unstable mode that agrees with the observations. In the numerical simulations, attention has been devoted to features resembling monochromatic gravity waves since these are most easily identified as gravity waves (both by visual inspection and by quantitative comparison with linear wave theory through the evaluation of polarization and dispersion relations).

Recent investigations have demonstrated, however, that linear gravity waves generated by a steady heat source can cause disturbances that have little resemblance to the canonical picture of a monochromatic internal gravity wave (Bretherton 1988; Nicholls et al. 1991; Pandya et al. 1993). An example of the flow in this type of disturbance is shown in Fig. 2, which was calculated using the Boussinesq equations linearized about a horizontally uniform basic state at rest. The heat source is confined to a compact region 10 km deep centered at $x = 0$ [given by (6) in Nicholls et al. 1991], and, as shown in Fig. 2, it generates a circulation with low-level flow directed toward the heat source and an upper-level flow directed away from the heating. Since these are linear solutions in a basic state with no mean wind, the advection of momentum plays no role in the development of this circulation. The speed at which the leading edge of the circulation propagates to the left is governed by a gravity wave group velocity and is independent of the magnitude of the velocity extrema in the upper and lower branches of the flow. Some confusion may arise in applying the term gravity wave to the disturbance in Fig. 2 since the region behind the wave front is almost horizontally homogeneous and does not resemble a simple wave. If the heating were switched off, however, the disturbance would have a trailing edge propagating leftward at the same speed as the leading edge and would be easily recognizable as a wave pulse. Since the underlying dynamics are the same whether or not the heat source is switched off, we refer to the disturbance shown in Fig. 2 as a gravity wave.

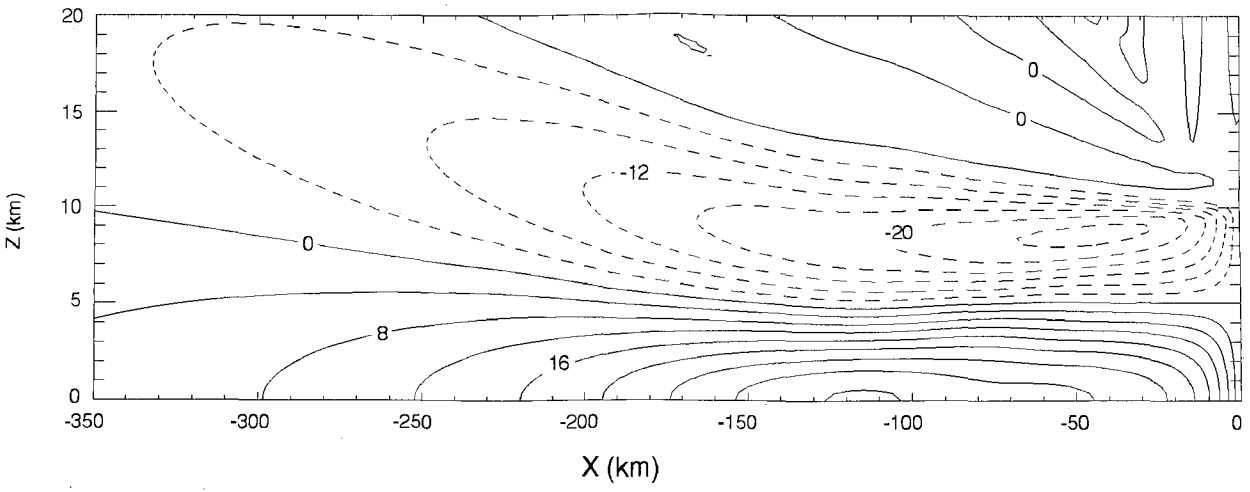

FIG. 2. Horizontal velocity (contoured in 4 m s^{-1} intervals) at $t = 2$ h generated by a compact heat source in a linear model.

Squall lines form in environments that are conditionally unstable. One might suppose, therefore, that any cloudy region within the leading line or trailing anvil might be statically unstable. In fact, most of the interior of the system is stably stratified, including much of the leading line. This can be seen in Fig. 3, which is a contour plot of the Brunt–Väisälä frequency within a two-dimensional numerical simulation of a squall line. (Details of the numerical model used to generate this storm will be discussed in section 2.) In saturated regions, the conventional formula for the Brunt–Väisälä frequency was modified to take into account the effects of latent heat release on the static stability (Durran and Klemp 1982), in which case

$$N_m^2 = \begin{cases} g\left\{\dfrac{1+(Lq_s/RT)}{1+(\epsilon L^2 q_s/c_p RT^2)}\left(\dfrac{d\ln\theta}{dz}+\dfrac{L}{c_pT}\dfrac{dq_s}{dz}\right) - \dfrac{dq_w}{dz}\right\} & \text{if } q_v \geq q_s \\ g\left(\dfrac{d\ln\theta}{dz}\right) & \text{otherwise,} \end{cases} \quad (1)$$

where q_v is the mixing ratio of water vapor, q_s is the saturated mixing ratio of water vapor, and q_w is the mixing ratio of all hydrometeors.[1] The outline of the cloud, defined by regions in which the cloud liquid water mixing ratio exceeds 1.0 g kg^{-1}, is also plotted as the thick line in Fig. 3. The only persistent areas of negative Brunt–Väisälä frequency (which appear as darkly shaded regions) are in the well-mixed boundary layer and in the low-level core of the main updraft. There are also a few small transient regions of negative N_m within the stratiform anvil, but Fig. 3 indicates that the bulk of the leading line–trailing anvil system is stably stratified. Gravity waves can, therefore, propagate throughout essentially the entire system.

2. The numerical model

a. Governing equations

The squall line simulations presented in this paper were performed using a two-dimensional version of the cloud model used in Miller and Durran (1991). This is a nonhydrostatic and fully compressible model, employing the warm rain bulk microphysics used in the Klemp and Wilhelmson (1978) cloud model. The governing equations for this model are the momentum equations

$$\frac{\partial(\rho u)}{\partial t}+\frac{\partial(\rho u^2)}{\partial x}+\frac{\partial(\rho uw)}{\partial z}+\frac{\partial p}{\partial x}=\rho D_u \quad (2)$$

$$\frac{\partial(\rho w)}{\partial t}+\frac{\partial(\rho uw)}{\partial x}+\frac{\partial(\rho w^2)}{\partial z}+\frac{\partial p}{\partial z} = -(\rho-\bar{\rho})g+\rho D_w, \quad (3)$$

a prognostic pressure equation derived from the continuity equation

$$\frac{\partial p}{\partial t}+\frac{c_p p}{c_v \rho}\left[\frac{\partial(\rho u)}{\partial x}+\frac{\partial(\rho w)}{\partial z}\right]=\frac{c_p p}{c_v \theta}\frac{\partial\theta}{\partial t}, \quad (4)$$

and the thermodynamic equation

$$\frac{\partial\theta}{\partial t}+u\frac{\partial\theta}{\partial x}+w\frac{\partial\theta}{\partial z}=Q+D_\theta. \quad (5)$$

[1] L is the latent heat of vaporization for water, c_p is the specific heat of dry air at constant pressure, R is the ideal gas constant for dry air, ϵ is 0.622, T is the sensible temperature, θ is the potential temperature, and z is the vertical coordinate.

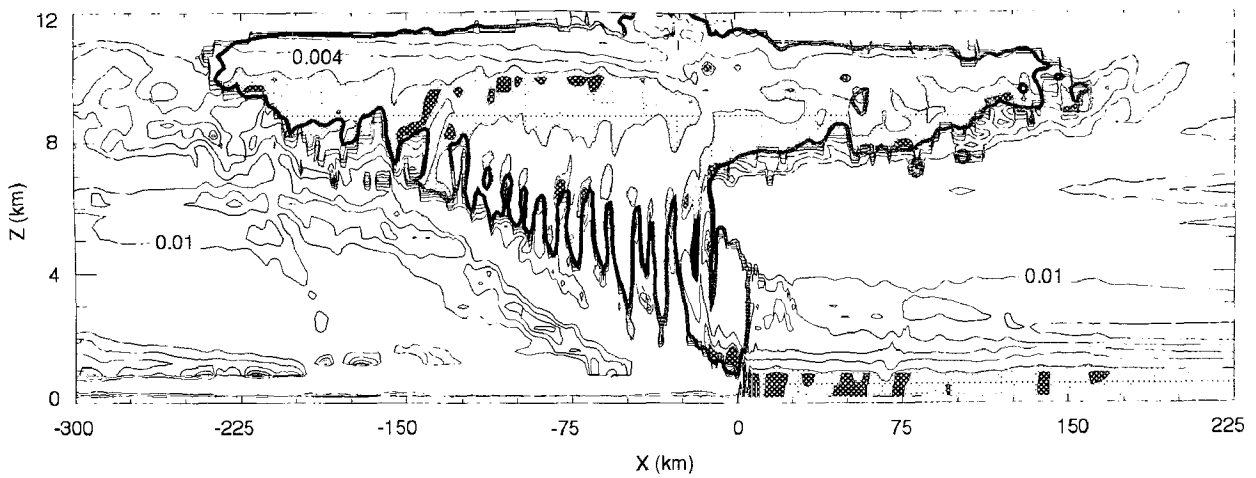

FIG. 3. Brunt–Väisälä frequency (contoured in 0.002 s^{-1} intervals) in a numerically simulated squall line. Cloud outline is indicated by the heavy contour. Dark shading indicates statically unstable regions. Light shading appears where $N < 0.002\ s^{-1}$.

The D_u, D_w, and D_θ terms in (2), (3), and (5) denote the subgrid-scale mixing determined using the Richardson-number-dependent first-order closure scheme described in Durran and Klemp (1983). The term $\bar{\rho}$ in (3) is the mean state density. In (5) Q represents a diabatic heat source, either applied externally or computed as the result of microphysical processes; u, v, and w are wind components in the x, y, and z directions, and p is pressure. This system is completed by the equation of state and the continuity equations for water, which are given in Durran and Klemp (1983).

Equations (2)–(5) were integrated using a two-time-step scheme (Klemp and Wilhelmson 1978; Skamarock and Klemp 1992) in which a small time step was used to stably integrate the terms involving high-speed sound waves and a larger time step was used for other terms. The model domain was 700 km wide by 22 km high, with a horizontal resolution of 1000 m and a vertical resolution of 350 m. The small time step was 2 seconds, and the large time step was 6 seconds. The upper and lateral boundaries were open, allowing waves to propagate out of the computational domain with minimal spurious reflection. Perturbations in u and θ were advected outward through the lateral boundaries at fixed phase speeds equal to the Doppler-shifted phase speed of the gravest gravity wave mode (Pearson 1974; Durran et al. 1993). The radiation upper-boundary condition followed Klemp and Durran (1983) and Bougeault (1983).

b. Initial conditions

The reference simulation was initialized with horizontally uniform profiles of wind, temperature, and moisture based on observations of the prestorm environment of the 22 May 1976 squall line that passed through the mesonetwork of the National Severe Storms Laboratory in central Oklahoma (Ogura and Liou 1980). The thermodynamic sounding is shown in Fig. 4a; it is a smoothed version of the 1430 CST sounding at station HNT. In addition to the smoothing, the thermodynamic profile has been modified by warming and moistening the layer between the surface and ~850 mb. This modified sounding is identical to the one used in a previous numerical simulation of the 22 May 1976 squall line performed by Fovell and Ogura (1988); it has a CAPE (convective available potential energy) of ~2400 J kg^{-1}. Figure 4b shows the storm-relative mean horizontal wind used in the reference simulation. It is also similar to the wind profile presented in Fovell and Ogura (1988) but is smoothed to eliminate discontinuities in the wind shear. Even with this smoothing, the low-level shear in the reference state wind profile remains comparable to that observed in the prestorm environment on 22 May 1976 (Ogura and Liou 1980). Convection in the reference simulation was initiated using a 2 K warm bubble near the surface.

3. Mesoscale velocity perturbations

a. Horizontal velocity perturbations

This section examines the evolution of the horizontal velocity perturbations in the mesoscale region surrounding the leading convective line. As shown in Fig. 1, the observed flow in the trailing stratiform region can be divided into two primary currents: an upper-level ascending front-to-rear flow (FTRF) and a mid-level descending rear inflow (RI). Figure 1 also shows an upper level rear-to-front flow ahead of the convective line. This feature, often associated with a forward-spreading cloud anvil, will be referred to as the leading anvil flow (LAF).

In the remainder of this section, two numerical simulations are compared to illustrate the role that gravity

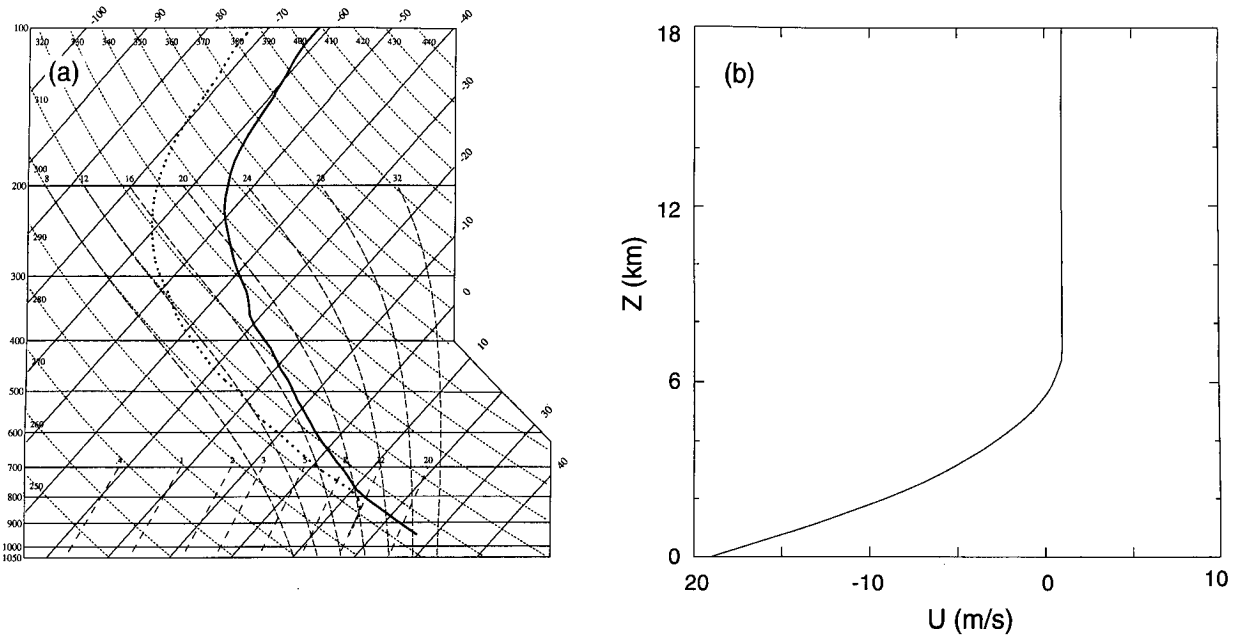

FIG. 4. The initial sounding used in the reference and dry simulations: (a) skew T diagram showing the temperature (solid) and dewpoint temperature (dashed); (b) vertical profile of the horizontal wind speed.

waves forced by the latent heating and cooling in and near the leading convective line play in the development and maintenance of the horizontal velocity perturbations in the mesoscale region around convection. The first of these simulations, the reference simulation, is a complete simulation that employed a parameterization of warm cloud microphysics. The second simulation presented here was performed with the microphysical parameterizations switched off; instead, the circulation was generated by a steady thermal forcing.

1) TIME-AVERAGED STRUCTURE

Figure 5a shows a 30-min time average of the storm relative horizontal velocity that develops in the mature stage of the reference simulation. The time average was taken to eliminate some of the small timescale features of the flow and thereby facilitate the comparison of the simulated flow and the conceptual model presented in Fig. 1. The light and dark shading highlight regions of strong negative and positive velocity, respectively.

As shown in Fig. 5a, the time-averaged flow in the reference simulation is similar to that in the conceptual model of a squall line with trailing stratiform precipitation presented in Fig. 1. The FTRF begins just above the gust front (x = 0 km) and ascends as it moves rearward. Beneath the FTRF the RI extends rearward from the gust front. The region ahead of the convection in Fig. 5a also shows a similarity to the conceptual squall line; both the upper-level cloud edge and the rear to front flow indicate a LAF.

The flow shown in Fig. 5a is also consistent with observations of the 22 May 1976 squall line. The 27 m s^{-1} maximum speed in the FTRF is similar to the 25 m s^{-1} maximum reported by Smull and Houze (1987a) in their dual Doppler analysis of the 22 May 1976 squall line. The RI in Fig. 5a reaches a maximum value in excess of 15 m s^{-1}, which agrees with the 17 m s^{-1} peak reported by Smull and Houze (1987b). In Fig. 5a the LAF extends ~120 km ahead of the convection and includes a region with forward-directed velocities exceeding 9 m s^{-1}. This is in broad agreement with Ogura and Liou (1980), who show a 110-km wide region of rear to front flow exceeding 10 m s^{-1}.

A series of numerical simulations were performed to test the sensitivity of the kinematic features in the trailing anvil to the heating and cooling in the region of the leading convective line. These simulations were performed using the same initial conditions and the same numerical model, but they were performed "dry," that is, with the microphysical parameterizations turned off. Sensitivity tests performed using the dry model show that the mesoscale circulation around the squall line is primarily generated by the low-frequency components of the thermal forcing. A good approximation to the mesoscale circulation surrounding the squall line can be generated by a steady thermal forcing of the form shown in Fig. 6a. This thermal forcing was constructed by time averaging and smoothing the latent heating and cooling in the reference simulation. The heating and cooling in the reference simulation was averaged over

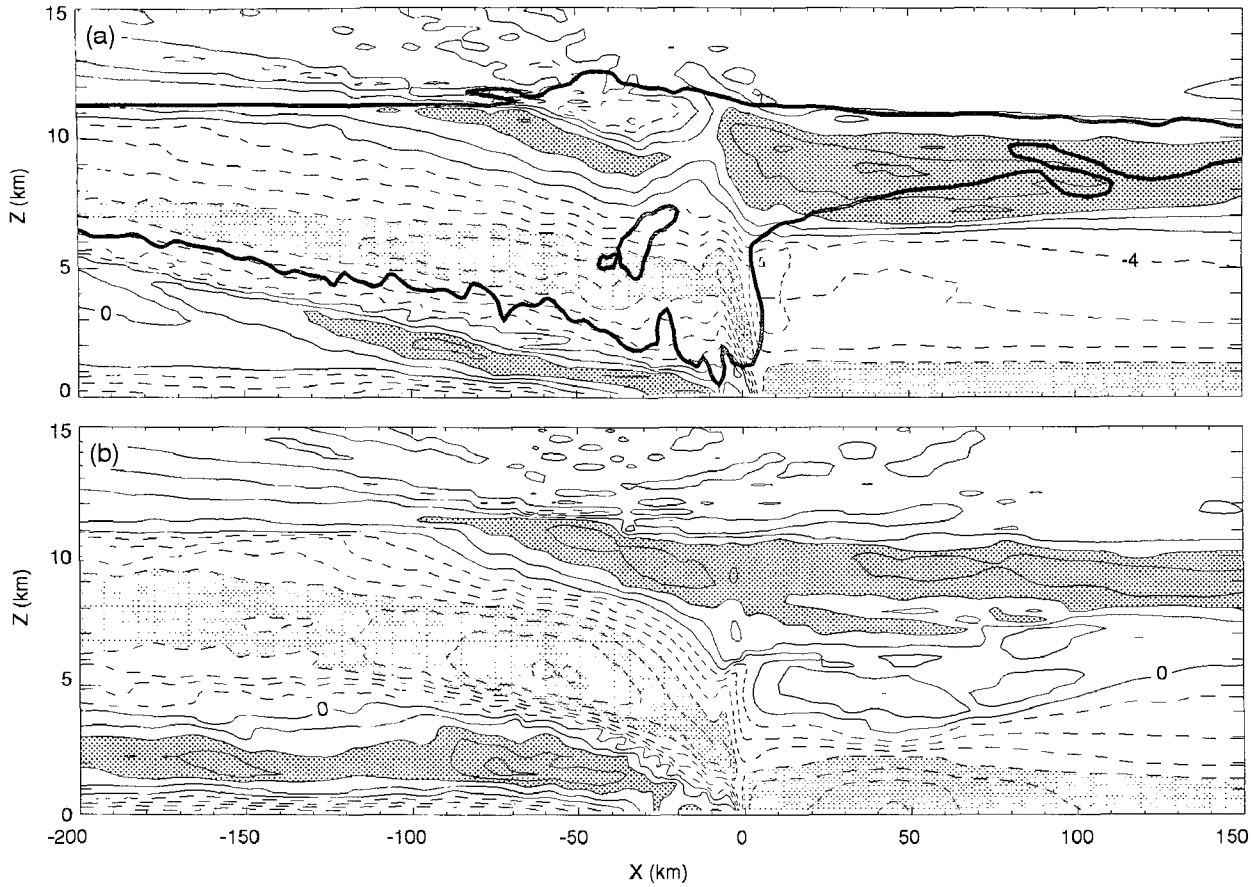

FIG. 5. (a) Time-average system-relative horizontal velocity (thin lines, contoured in 4 m s^{-1} intervals) in the reference simulation. Time-average is taken from 7.5 to 8 hours. Dark shading highlights rear to front flow greater than 8 m s^{-1}; light shading highlights front to rear flow with speed exceeding 16 m s^{-1}. Cloud outline (q_c = 0.1 g kg^{-1}) is indicated by the heavy line. (b) Time-average horizontal velocity taken from t = 5.5 to 6 h in the dry simulation. Shading and contours are as in (a).

the period from 4.5 to 6.5 hours in order to obtain a pattern representative of the mature phase of the squall line and eliminate the signature of individual convective cells. In order to keep the thermal forcing compact, the thermal forcing was set to zero at all points where its magnitude was less than 0.0001 K s^{-1}. The residual cellular structure was removed by running the time-averaged field through a second order smoother 200 times, and the resulting field was scaled so that its integrated absolute value matched the integrated absolute value of the time-averaged field. The instantaneous heating and cooling in the reference simulation at time t = 6 h is shown in Fig. 6b for comparison.

Figure 5b shows the horizontal velocities generated by the thermal forcing shown in Fig. 6a. Although the thermal forcing is steady and smooth, the dynamical response to this forcing is neither steady nor smooth. As in Fig. 5a, the horizontal velocities in Fig. 5b have been averaged over a 30-min interval in order to emphasize the slowly varying structures in the flow. This 30-min average was taken from 5.5 to 6.5 hours, two hours earlier than the time average shown in Fig. 5a, in order to account for the slower initiation and early evolution of the squall line in the reference simulation, during which time the pattern of latent heating and cooling differed from that in the mature phase.

The horizontal flow presented in Fig. 5b is qualitatively similar to the flow in both the reference simulation and the schematic diagram of a squall line shown in Fig. 1. A pronounced FTRF begins near the gust front (x = 0 km) and ascends rearward, and a region of RI occurs beneath it. An upper-level LAF is visible in the region $z > 8$ km and $x > 0$ km. The presence of these flows in the dry simulation suggests that the large-scale horizontal circulation in the stratiform region behind the squall line arises primarily in response to the thermal forcing generated at the system's leading edge.

The RI in the dry simulation shows a pronounced bimodal structure, with two regions of stronger inflow separated by an area of weaker inflow. In Fig. 5b, a local maximum in the inflow is centered at $x \sim -150$ km and another stronger maximum inflow extends from

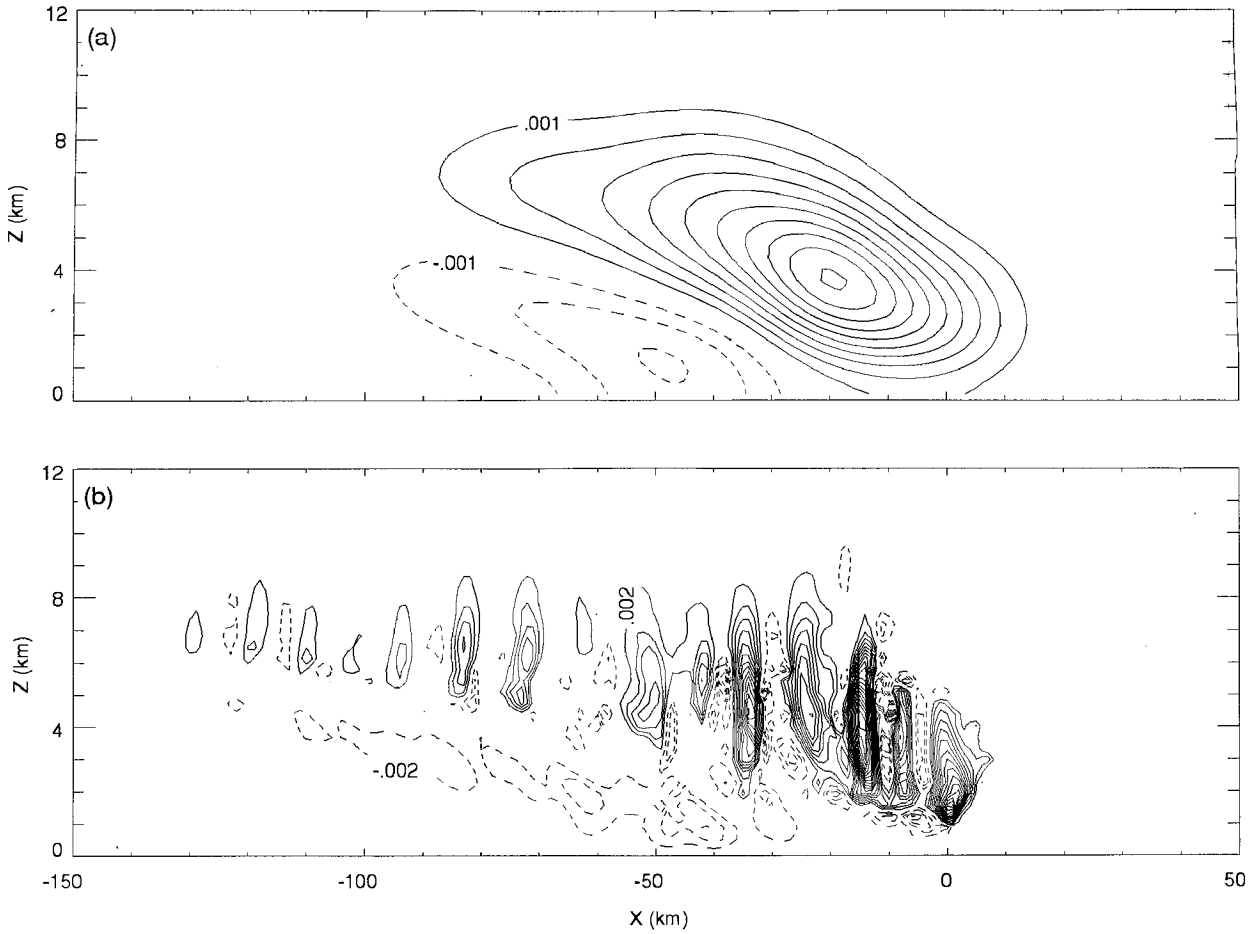

FIG. 6. (a) Thermal forcing used in the dry simulation. Contour interval is 0.001 K s^{-1}. (b) Instantaneous pattern of heating and cooling in the reference simulation; contour interval is 0.002 K s^{-1} at $t = 6$ h.

$x \sim -90$ km to the gust front. This bimodality in the amplitude of the RI was also observed in the stratiform region trailing the 22 May 1976 squall line [see Fig. 13 of Ogura and Liou (1980) and Fig. 9 of Smull and Houze (1985)]. A bimodal RI with a maximum inflow located immediately to the rear of the convective line and a second maximum at the back edge of the trailing stratiform anvil is common in leading line–trailing anvil systems (Smull and Houze 1987b). Some studies have suggested that the formation of the second maximum at the back edge of the trailing anvil results, at least partly, from local cooling (Smull and Houze 1987b; Yang and Houze 1995b). The results of the dry simulation indicate that some bimodality in the RI can, nevertheless, be generated solely by the mean thermal forcing at the system's leading edge.

Although the location and qualitative structure of the circulation features match in the dry and reference simulations, a close comparison of Figs. 5a and 5b reveals that the wind speeds are somewhat larger in the dry simulation in spite of the fact that the absolute amplitude of the thermal forcing in the two simulations was the same. In the dry simulation, the circulation was generated by a thermal forcing that was constant in time, whereas the circulation in the reference simulation was generated by a time-varying thermal forcing associated with the release and absorption of latent heat by active convection. The steady thermal forcing in the dry simulation projected more directly onto the low-frequency gravity waves that determine the mesoscale circulation, while the time-varying thermal forcing in the reference simulation projected relatively more energy onto high-frequency modes less important to mesoscale circulation. Thus, since the amplitude of the thermal forcing was the same in the two simulations, the dry simulation had more amplitude in the low-frequency modes and a stronger mesoscale circulation.

Although most large-scale features of the dry and reference simulation agree, there are some differences worth noting. In the dry simulation there is a region of rear to front flow between $x = 10$ km and $x = 60$ km and around $z = 6$ km that does not occur in the refer-

ence simulation. An explanation of this difference can be found in the evolution of the horizontal velocity field, which will be discussed in the next section.

2) EVOLUTION

Some insight into the dynamics governing the development of the mesoscale horizontal flows can be gained by examining the instantaneous horizontal velocity perturbations in the reference and dry simulations. Figures 7a and 7b show the instantaneous horizontal velocity in the reference simulation at $t = 4.5$ hours and $t = 6$ hours, respectively. In Fig. 7a there are two distinct upper level extrema, features 1 and 3, that quickly move out of the model domain so that neither is visible in Fig. 7b. (Note that features 1 and 3 have a signature that extends all the way to the surface, although both features are weak at low levels and hard to identify because of the strong low-level mean wind.) Features 1 and 3 are fast-moving transient gravity wave modes generated by the thermal forcing in the convective region. The tilt of features 1 and 3 is consistent with gravity waves transporting energy upward and away from the convective region, and their speed of propagation is the same as the phase speed of hydrostatic gravity waves with a vertical half-wavelength of about 8.5 km, which is approximately equal to the 8-km depth of the convective cells.

While features 1 and 3 quickly propagate far away from the squall line, feature 2 moves at approximately the same speed as the downstream edge of the FTRF. Like features 1 and 3, feature 2 maintains its vertically upright structure as it propagates laterally from $x \sim -185$ km in Fig. 7a to $x \sim -315$ km in Fig. 7b. Horizontal velocity perturbations that include both an upper-level FTRF and a low-level RI immediately trail feature 2. Feature 2 and the velocity perturbations behind it together resemble the linear gravity wave response to a steady and compact thermal forcing shown in Fig. 2. Thus, although the RI and FTRF do not look like canonical monochromatic gravity waves, they appear to be a gravity wave response to the convective

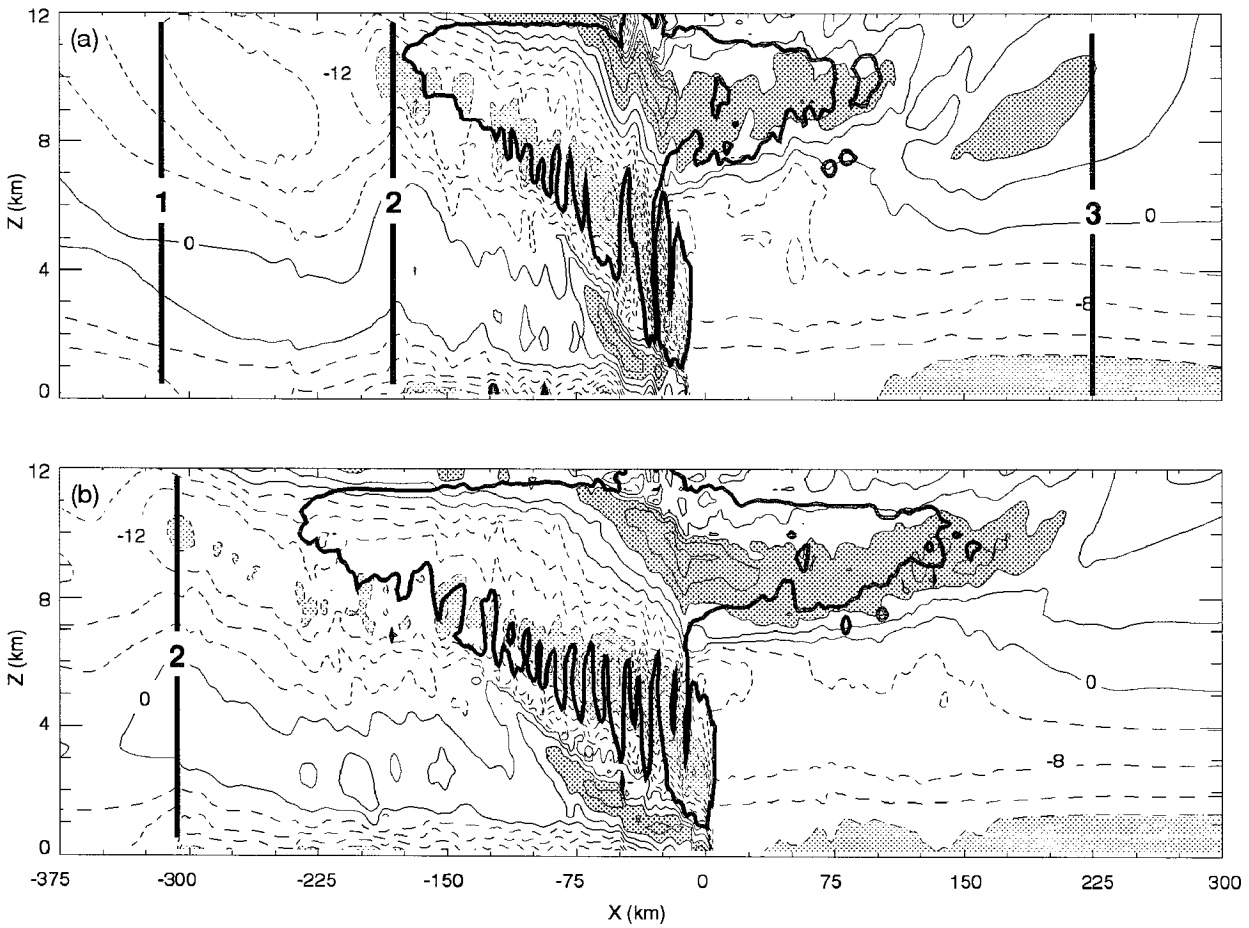

FIG. 7. Snapshots of the horizontal velocity in the reference simulation at (a) $t = 4.5$ h and (b) $t = 6$ h. Contours and shadings are as in Fig. 5. Cloud outline is indicated by the heavy line.

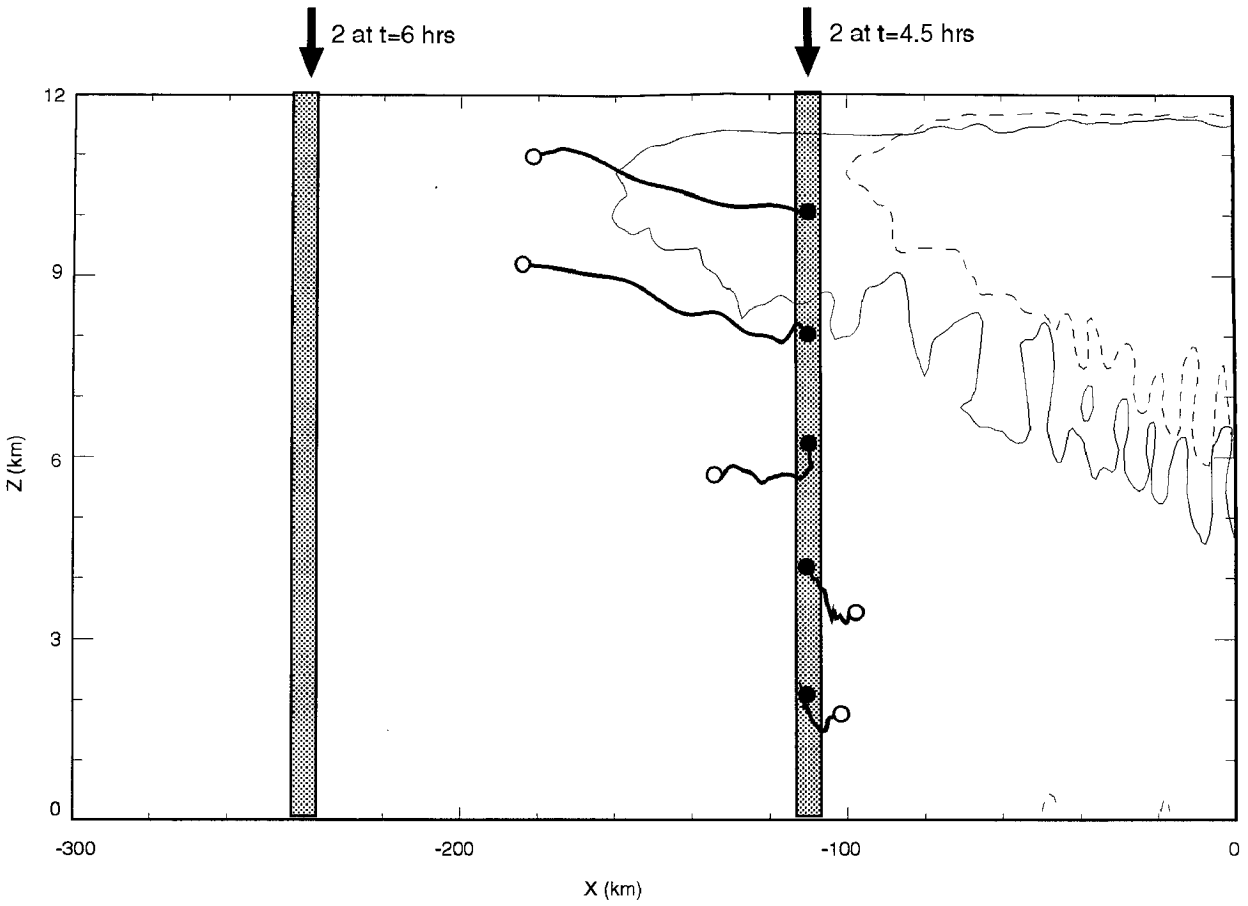

FIG. 8. Trajectories (thick solid lines) from $t = 4.5$ (closed circles) to $t = 6$ hours (open circles) in the reference simulation. Cloud outline is indicated at $t = 4.5$ h (thin dashed lines) and $t = 6$ h (thin solid lines).

thermal forcing. Notice that feature 2 and the RI and FTRF behind it propagate more rapidly than the cloud edge, implying that the FTRF and RI are not directly forced by in situ microphysical processes in the stratiform region.

Simple advection cannot explain the fact that feature 2 retains its coherent vertical structure as it propagates. This can be seen in Fig. 8, which compares the propagation of feature 2 with the trajectories of air parcels initially within feature 2. The trajectories begin at $t = 4.5$ h at 2-km vertical intervals along the line $x = -185$ km, and end 1.5 hours later at the open circles. The propagation of feature 2 over the same interval is indicated by the two labeled shaded lines. Feature 2 propagates faster than any of the parcels initially within it, which is inconsistent with advection. Furthermore, advection along the trajectories indicated would tend to destroy the vertical structure, but, as shown in Fig. 7, feature 2 maintains its vertical structure. Since there is no active convection in this region, and therefore no thermal forcing, and since the movement of feature 2 cannot be attributed to advection, the motion of feature 2 must be the result of gravity wave propagation.

Figure 9 shows the time evolution of the flow in the dry nonlinear simulation over a 1.5-h period. As in the reference simulation, shown in Fig. 7, a pair of upper-level outrunning horizontal velocity extrema (features 1 and 3 in Fig. 9a) develop in the dry simulation and quickly move out of the domain by the time shown in Fig. 9b. While the structure and speed of propagation of these features agree in the two simulations, feature 3 seems to have greater amplitude at midlevels in the dry simulation. This difference is the result of differences in thermal forcing early in the simulations. The dry simulation used a steady heat source that was switched on suddenly at $t = 0$, while the heating in the reference simulation evolved gradually. The amplitude of feature 3 was appreciably less in additional dry simulations in which the thermal forcing was turned on gradually.

As in the reference simulation, the spread of the horizontal velocity perturbations in the stratiform region appears to be linked to the propagation of feature 2. In

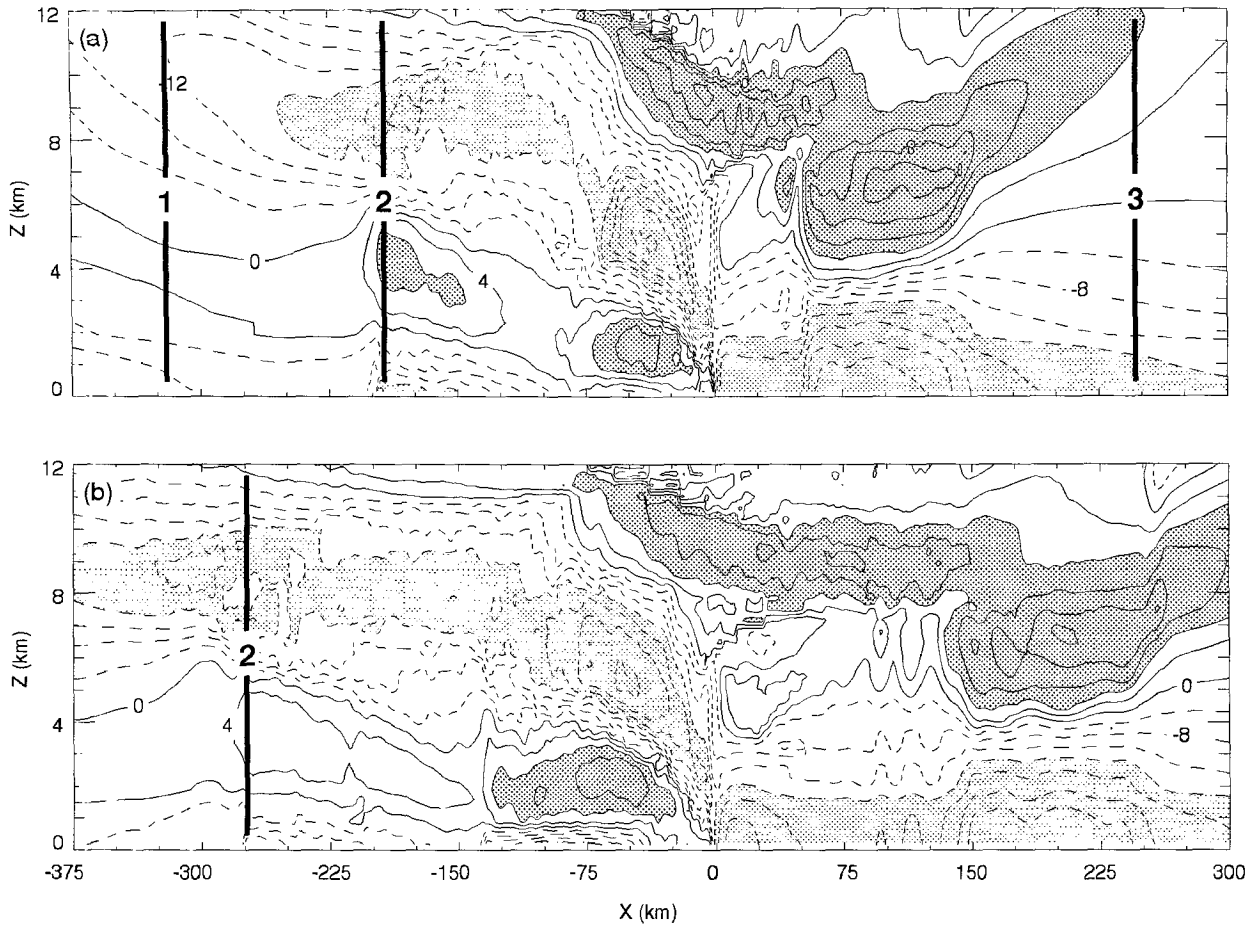

FIG. 9. Snapshots of the horizontal velocity in the dry simulation at (a) $t = 2.5$ h and (b) $t = 4$ h. Contours and shadings are as in Fig. 5.

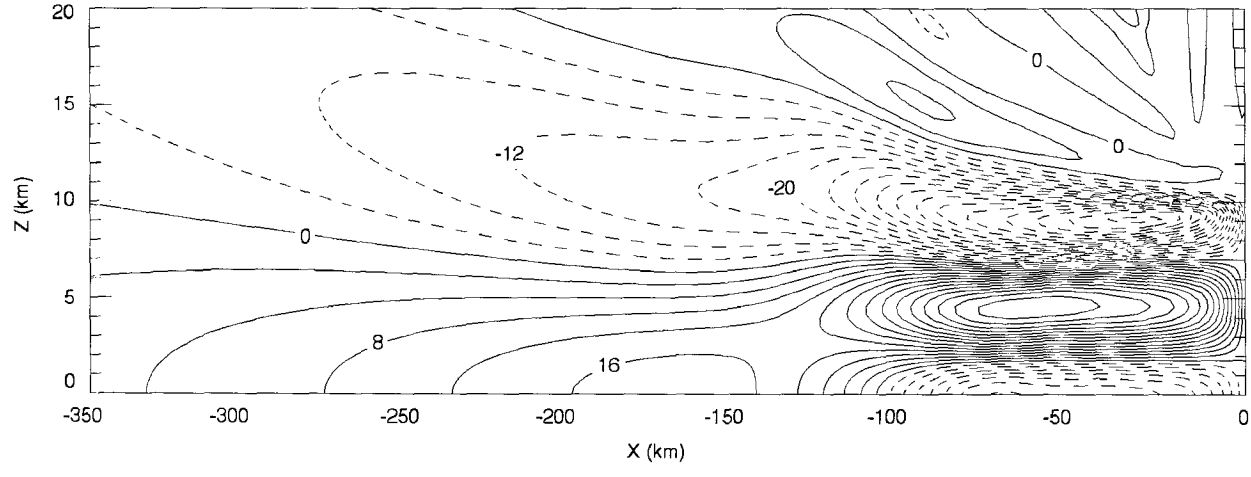

FIG. 10. Horizontal velocity (contoured in 4 m s^{-1} intervals) at $t = 2$ h generated by a compact heat source that forces two different modes in a linear model.

both simulations feature 2 maintains its vertical structure as it propagates through regions of pronounced vertical shear and leaves velocity perturbations in its wake that include the FTRF and RI. The propagation of feature 2 and the velocity perturbations behind it are again reminiscent of the linear gravity wave response to a compact heat source as shown in Fig. 2. This suggests that the FTRF and RI are indeed part of the gravity wave response to the time-mean thermal forcing.

Examining the evolution of the flow in the reference simulation (Fig. 7), one might suppose that features 1 and 3 are forced by an early profile of the thermal forcing from the leading line, and feature 2 is the response to the thermal forcing of the mature state. This idea is, however, refuted by the presence of features 1 and 3 in the dry simulation (Fig. 9), in which the thermal forcing is constant in time. Instead, the formation of distinct features in the trailing anvil is the result of the horizontal dispersion of different gravity wave modes. In both the reference and dry simulations, features 1, 2, and 3 mark individual contour lines associated with disturbances that extend over a large horizontal distance, so these disturbances are approximately hydrostatic. The horizontal phase speed and the horizontal group velocity of hydrostatic, Boussinesq gravity waves are identical and equal to N/m where N is the Brunt–Väisälä frequency and m is the vertical wavenumber. Since the horizontal group velocity and phase speed are identical, the displacement of any particular contour (not just a maxima and minima) will give an indication of the speed of the wave associated with the feature. In both the reference and dry simulations, feature 2 travels at $\sim$14 m s^{-1}, which is the speed of a hydrostatic wave whose $\sim$8.5-km vertical wavelength is comparable to the depth of the thermal forcing. Features 1 and 3 propagate at $\sim$28 m s^{-1}, which is the speed of a wave with a vertical wavelength twice the depth of the thermal forcing. The dispersion of modes with different vertical wavelengths is illustrated by the simple linear simulation shown in Fig. 10. This simulation is identical to the linear simulation shown in Fig. 2, except that the vertical structure of the heat source is composed of two modes whose vertical wavelengths differ by a factor of 2 (see Fig. 4 of Nicholls et al. 1991). The superposition of these modes resembles the profile of diabatic heating associated with leading line–trailing stratiform systems (Houze 1982; Johnson and Young 1983; Mapes 1993). The horizontal velocity perturbations that develop in response to this forcing show two distinct modes propagating at different speeds that are analogous to features 1 and 2 in Figs. 7 and 9.

It is worth pointing out that in both the reference and dry simulations feature 2 moves at the same speed as the rearward-traveling edge of the low-level cold pool. (The cold pool can be inferred from Figs. 7 and 9 by the negative velocities at the surface behind the gust front.) An additional simulation was performed that was identical to the reference simulation, except that the low-level cold pool was limited to $x > -175$ km by relaxing the temperature perturbations below 1.5 km and to the rear of $x = -175$ km back to the initial unperturbed values. Neither the upper-level structure nor the speed of propagation of feature 2 was significantly changed in this simulation, suggesting that the feature 2 is not dependent on the rearward spreading cold pool but is a consequence of the thermal forcing from the leading line.

b. Mesoscale vertical motions

1) TIME-AVERAGED VERTICAL VELOCITIES

Ogura and Liou (1980) observed a region of ascent $\sim$ 90 km wide centered at 400 mb and a wide region of descent $\sim$ 65 km centered at 850 mb in the stratiform region of the 22 May 1976 squall line. The vertical velocities seem relatively smooth in their analysis, which was based on composite soundings, but finer-scale Doppler radar observations by Smull and Houze (1987a) reveal cell-like perturbations in the vertical velocity field. Figure 11a shows the vertical velocity field in the reference simulation, time averaged from 8 to 10 hours. There is a broad, continuous region of mesoscale ascent stretching $\sim$80 km behind the gust front ($x = 0$ km). Farther to the rear, the vertical velocity field appears more cellular. These cell-like updrafts exceed 0.8 m s^{-1}, comparable to the $>$0.6 m s^{-1} maximum reported by Ogura and Liou (1988) $\sim$100 km behind the convection (they show a contour at -0.03 mb s^{-1} at 400 mb in their Fig. 16). Nearer to the region of convection, the vertical velocity exceeds 6.4 m s^{-1}, consistent with the 10 m s^{-1} measured by Smull and Houze (1987a). A region of mesoscale descent is visible behind the gust front and below the mesoscale updraft. The magnitude of the descent exceeds 0.4 m s^{-1}, consistent with the 40 cm s^{-1} downdraft observed by Ogura and Liou (1980) (contoured as 0.04 mb s^{-1} downdraft at 850 mb in their Fig. 16).

Figure 11b shows the time-averaged vertical velocity that develops in the dry simulation driven by the thermal forcing shown in Fig. 6a. Here the time average was taken from $t = 6$ to 8 h, which is two hours earlier than the interval shown in Fig. 11a. The 2-h offset accounts for the gradual development of the convection early in the reference simulation, as discussed in section 3a(1). In agreement with the reference simulation, the mesoscale ascent in the dry simulation is continuous near the gust front ($x = 0$ km) and more cellular farther to the rear, and a broad region of mesoscale descent is apparent beneath the mesoscale updraft. Although the vertical velocity fields agree qualitatively in the two simulations, the magnitudes of the vertical velocities in the dry simulation systematically exceed those in the reference simulation. This is because, as discussed in section 3a(1), the steady thermal forcing in the dry

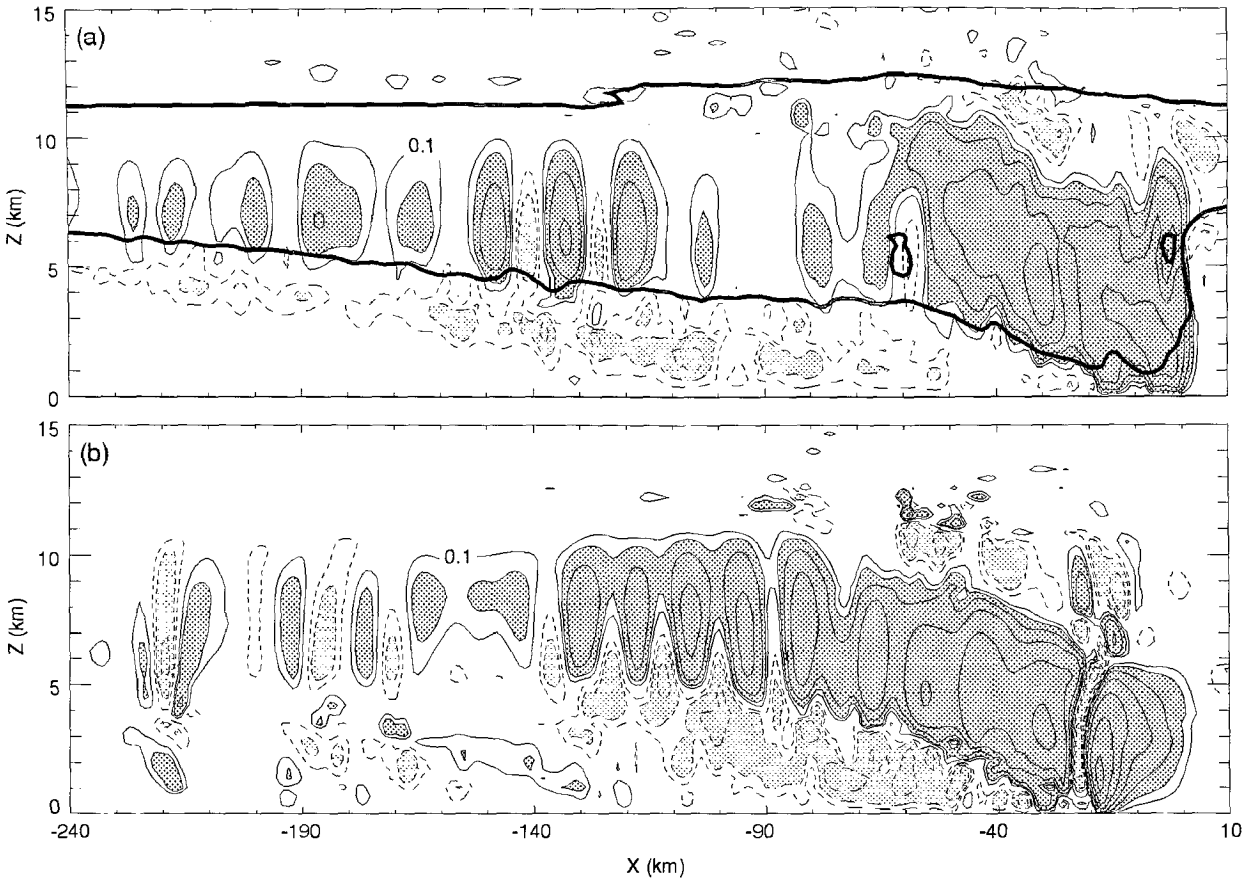

FIG. 11. (a) Time-averaged vertical velocity (thin lines, contours are $w = \pm 0.1, \pm 0.2, \pm 0.4, \cdots, \pm 6.4$ m s^{-1}) taken from $t = 8$ to 10 h in the reference simulation. Dark shading indicates upward velocity exceeding 0.2 m s^{-1}; light shading indicates downdrafts with speed exceeding 0.2 m s^{-1}. Cloud outline is indicated by the thick line. (b) Time-average vertical velocity taken from $t = 6$ to 8 h in the dry simulation. Contours and shadings are as in (a).

simulation projects more directly onto the low-frequency modes responsible for the mesoscale circulation than does the thermal forcing in the reference simulation.

In both the reference and dry simulations, the vertical velocity field shows more short horizontal wavelength structure than the horizontal velocity field, as can be seen by comparing Figs. 5a and 5b to Figs. 11a and 11b. For example, in the dry simulation, the FTRF extends smoothly well to the left of $x = -200$ km, while the mesoscale updraft shows a cellular structure for $x < -90$ km. These cell-like velocity features cannot be the result of local microphysical processes since they are also apparent in the dry simulation that did not include microphysical processes. The vertical and horizontal velocity perturbations in Boussinesq gravity waves are related by the polarization relation,

$$w_0 = \frac{-H}{L} u_0, \qquad (6)$$

where u_0 and w_0 are the amplitudes of the horizontal and vertical velocities, and H and L are the horizontal and vertical wavelengths, respectively. Equation (6), which can also be derived from scaling arguments applied to the continuity equation where H and L are horizontal and vertical length scales, implies that if two features have the same vertical scale and the same amplitude in the horizontal velocity perturbations, the feature with the shorter horizontal scale will be associated with the larger vertical velocity perturbations. Since the dominant vertical length scale in the horizontal and vertical velocity perturbations of the trailing anvil appears to be the same, the vertical velocity field should be expected to show more small-scale horizontal structure than the horizontal velocity field. Examining Fig. 11 reveals that the cells in the mesoscale updraft have a horizontal scale of ~10 km, a vertical scale of ~5 km, and an amplitude on the order of 0.5 m s^{-1}. Thus, according to (6), the horizontal velocity perturbations associated with this mode should have an amplitude of approximately 1 m s^{-1}. Although it is hard to see, Fig.

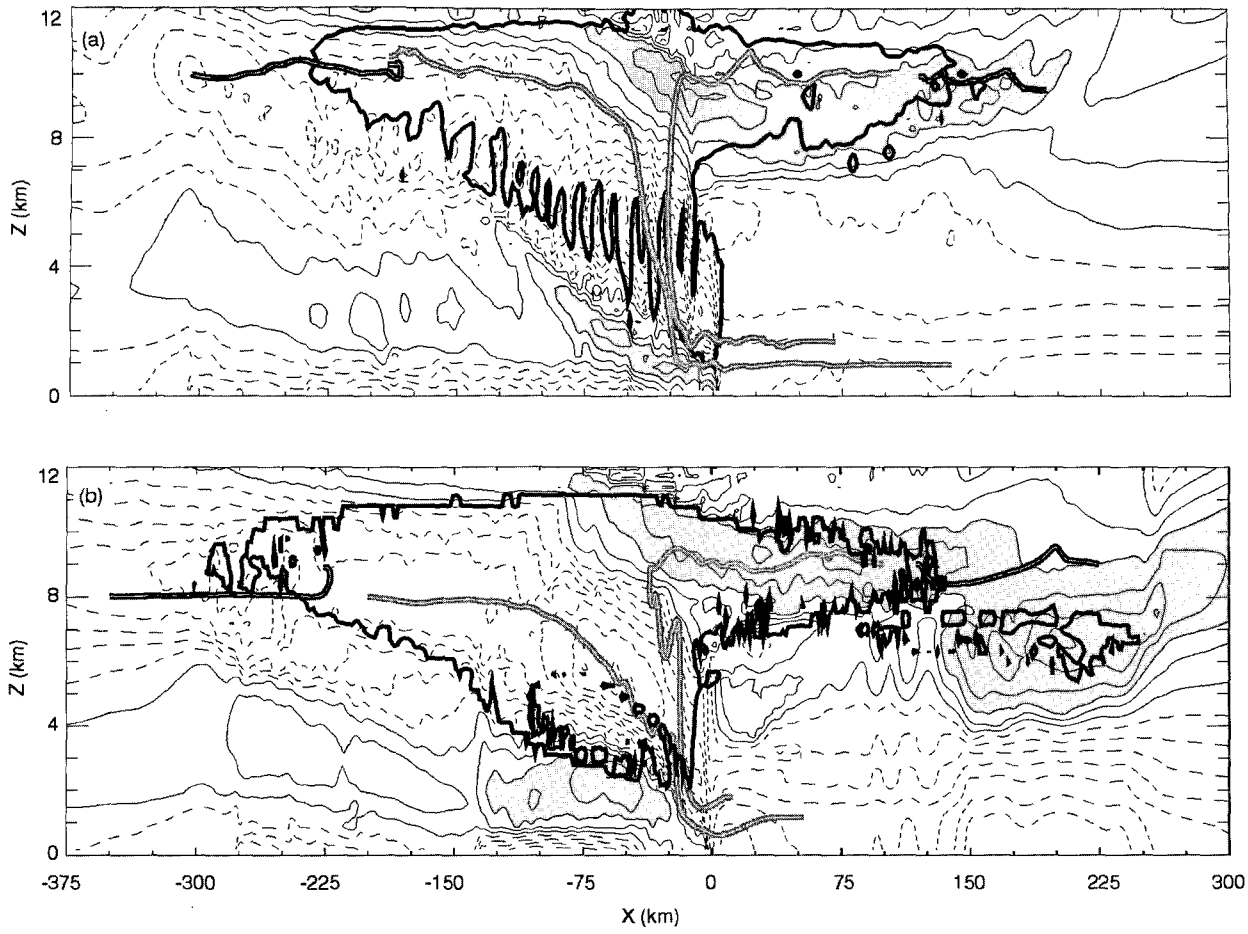

FIG. 12. (a) Instantaneous horizontal velocity (thin lines, intervals, and shading as in Fig. 5) at 6 hours in the reference simulation. Cloud outline is indicated by the heavier line. Trajectories of air parcels that end up within (outside) the cloud are indicated by the gray (black) double lines. (b) Instantaneous horizontal velocity (thin lines, intervals, and shading as in Fig. 5) at 4 hours in the dry simulation. The 2-km vertical-displacement contour is indicated by the heavier line. Trajectories of air parcels that end up within (outside) this region of enhanced vertical displacement are indicated by gray (black) double lines.

5 does indeed show weak small horizontal-scale modulations of the FTRF with a horizontal scale of ~10 km and an amplitude of ~1 m s^{-1}.

2) VERTICAL DISPLACEMENT

Although linear gravity waves propagate without producing a net air-parcel displacement, the finite-amplitude gravity waves forced by the convective line and discussed in section 3a(2) do generate a perturbed flow that produces a net air parcel displacement. All air parcel displacements generated in the squall line are not, however, produced by gravity waves. In particular, the large vertical displacements that occur as air in the convective region is lifted from the surface to the upper troposphere are driven by the diabatic heating of rising air parcels. The gravity wave and convectively driven displacements associated with squall lines are distinguished in Fig. 12a, which shows the horizontal velocity (thin lines) and cloud outline (thick line) at time 6 hours in the reference simulation. Overlayed on the velocity field are back trajectories of two air parcels within the cloud (double gray lines), one from the leading anvil and one from the trailing anvil. The back-trajectories reveal that both of these air parcels have undergone a diabatically driven ascent within the region of convection and were advected away from the convective region by the perturbed horizontal flow. Note that the perturbed horizontal flow, which was established as a gravity wave response to the thermal forcing in the convective line, extends well beyond the edge of the cloud. The back trajectories of air parcels that end up outside the cloud (double black lines) are much shorter than those ending up within the cloud and show no diabatically driven ascent; this is consistent

with the gravity wave interpretation of the spreading LAF and FTRF discussed in section 3a(2).

The cloud outline in Fig. 12a can be compared to the 2-km vertical-displacement contour in the dry simulation, indicated by the heavy line in Fig. 12b. Also shown in Fig. 12b are contours of the horizontal velocity field at time 4 hours. (As in Fig. 5 the 2-h offset between the dry and reference simulation was taken to account for the slower evolution of the squall line in the reference simulation.) The vertical displacement of an air parcel that ends up at the final position (x_f, z_f) at time $t = t_f$ is determined by first following the trajectory of that air parcel backward to time $t = 0$ to determine the initial position of the parcel (x_0, z_0). The vertical displacement is then given by $z_f - z_0$. If x_0 is beyond the right edge of the computational domain, z_0 is assumed to be the same as the height of the parcel when it entered the domain.

Comparing Figs. 12a and 12b reveals that the vertical displacement field in the dry simulation is most conducive to the production and transport of condensate into the regions where the trailing and leading anvils form in the reference simulation. Furthermore, the shape and vertical extent of both the leading and trailing features agree in the two simulations. As in the reference simulation, the air that undergoes large vertical displacement in the region of diabatic heating is advected by the perturbed flow at upper levels (as shown by the backward trajectories plotted as double grey lines), while the air parcels outside of the vertical-displacement boundary have back-trajectories (double black lines), suggesting that the motion of these air parcels was produced exclusively by gravity wave-induced velocity perturbations. In both the dry and reference simulations, the gravity waves excited by the thermal forcing produce the LAF and FTRF and these flows advect the diabatically heated and lifted air away from the region of heating. The similarity in the large-scale qualitative structure of the cloud in the reference simulation and the vertical displacement field in the dry simulation suggests that the gravity waves excited by the time-mean thermal forcing in the region of the leading convective line exert a dominating influence on the qualitative structure of the stratiform cloud.

4. Cloud-top temperatures

Ogura and Liou (1980) reported a broad horizontal region of negative temperature anomaly at ~200 mb in the stratiform region to the rear of the convection in their observations of the 22 May 1976 squall line and trailing anvil (see their Fig. 21). They attributed this cold anomaly to air parcels overshooting into the stratosphere. Gamache and Houze (1985) reported a similar negative temperature anomaly at upper levels of the trailing stratiform cloud and the cloud-free post-stratiform region behind the 12 September GATE squall line. Zipser (1988) compared satellite and radar data to show that the coldest cloud tops occurred well away from the region of most vigorous convection, suggesting that the stratiform cooling is not produced by the backward advection of air parcels that overshot their level of neutral buoyancy in the leading line. Johnson et al. (1990) suggested that the cold anomaly may be the result of enhanced IR cooling near cloud top. Similar regions of upper-level cooling are, however, generated in numerical simulations that do not include radiative processes. Fritsch and Brown (1982) used numerical simulations to conclude that the cold anomaly is the result of adiabatic expansion and cooling resulting from ascent within the trailing stratiform anvil. The simulations to be discussed in this section suggest that the adiabatic ascent occurs within gravity waves generated by the low-frequency component of the thermal forcing at the line leading edge of the squall.

Figure 13a shows the potential temperature perturbations that develop to the rear of the convective region in the reference simulation. The gust front is at $x = 0$ km. The negative cloud-top potential temperature anomaly reaches -6 K, comparable to the -6.5 K value reported by Ogura and Liou (1980) (plotted as a 4°C sensible temperature value in their Fig. 21). The spatial structure of the simulated cold region also agrees with the observations; in both cases the coldest air is located in a thin layer that begins ~50 km behind the gust front and extends rearward.

Figure 13b shows the potential temperature perturbation generated by the steady thermal forcing shown in Fig. 6a. A comparison of Figs. 13a and 13b reveals both qualitative and quantitative similarity between the dry and reference simulations; both exhibit an upper-level negative potential temperature anomaly centered around $z \sim 11$ km that stretches well behind the gust front. Notice that overshooting cloud tops, which are not present in the dry simulation, are not required to produce the upper-level cooling. Instead, the upper-level cooling develops as a result of adiabatic ascent in motions within gravity waves. The maximum value of the negative potential temperature anomaly in the dry simulation is -10 K. This is greater than the -6 K potential temperature maximum in the reference simulation, but, as discussed in section 3a(1), a stronger response develops in the dry simulation because the steady thermal forcing used in the dry simulation projects more directly onto the low-frequency gravity wave modes responsible for the mesoscale structure of the squall line. This hypothesis is supported by the fact that although the low-frequency modes have larger amplitude in the dry simulation, the high-frequency gravity wave modes have larger amplitude in the reference simulation. For example, the amplitude of the higher-frequency modes propagating through the region centered on $x = -100$ km, $z = 14$ km is largest in the reference simulation.

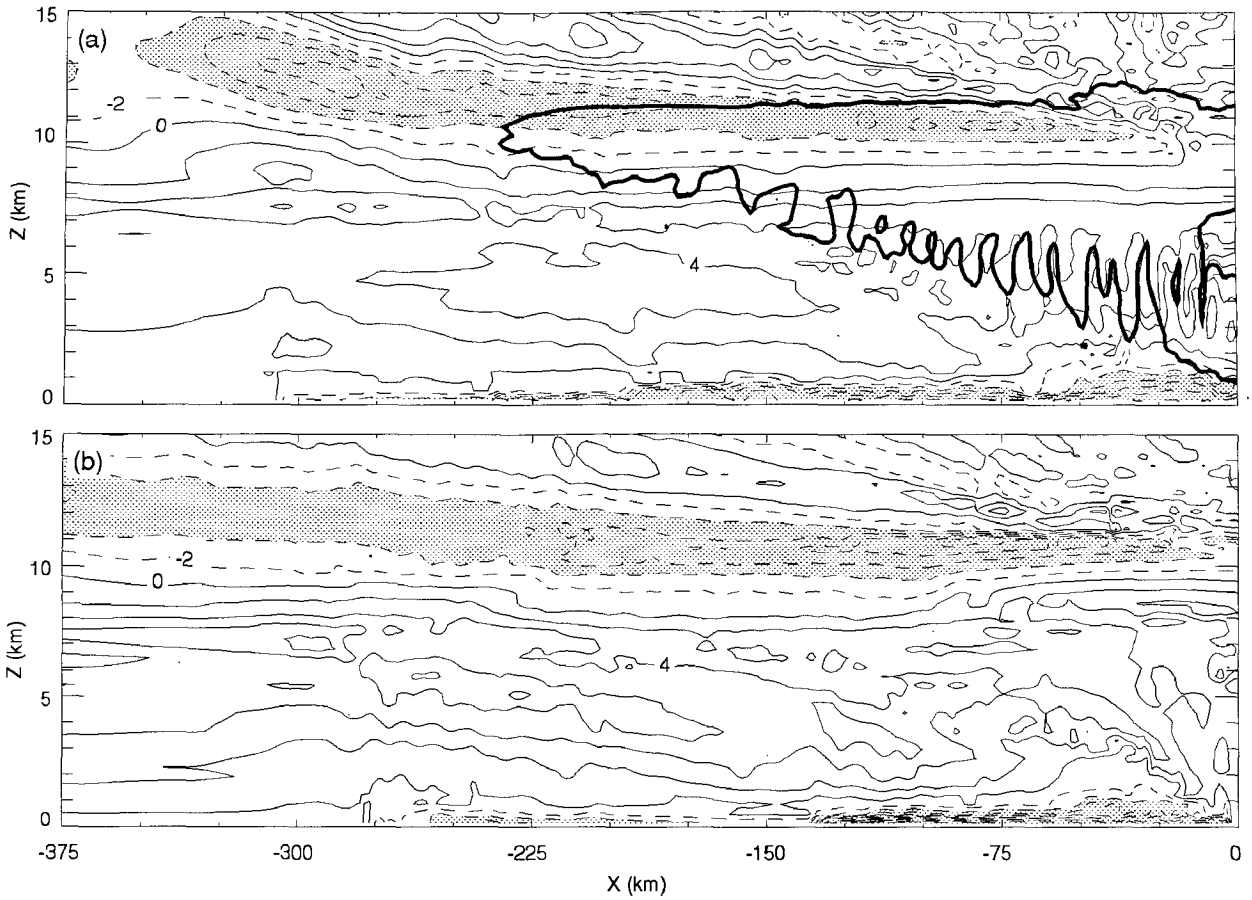

FIG. 13. Perturbation potential temperature (thin lines, contoured in 2-K intervals) at (a) $t = 6$ h in the reference simulation and (b) $t = 4$ h in the dry simulation. Areas where the potential temperature is less than −4 K are shaded. Cloud outline is indicated by the heavy line in (a).

Figure 13 shows that the upper-level potential temperature minimum in the stratiform and post-stratiform regions occurs as part of a larger-scale pattern of alternating bands of negative and positive potential temperature that extend up into the lower stratosphere. The slope of these bands is consistent with gravity waves transporting energy away from the convective region. The gravity wave structure of the lower stratosphere is particularly easy to recognize because the waves are almost monochromatic, as in the numerical simulations by Fovell et al. (1992). (The waves in the troposphere are harder to recognize because they are a superposition of many different modes.) For simple monochromatic vertically propagating plane parallel gravity waves, the extrema in the velocity field should be 90° out of phase with the extrema in the θ field. This phase shift can, in fact, be observed in Fig. 14, which compares the horizontal velocity and perturbation potential temperature in the reference simulation. A similar result holds for the dry simulation, although, as already discussed, the amplitudes of the perturbations are somewhat less above $z = 12$ km.

5. The development of updraft cells from a steady heat source

Observations and numerical simulations indicate that the convection in mature squall lines is often composed of a number of individual cells with horizontal and temporal scale much less than those of the squall line itself. Dudhia et al. (1987) reported that the cells in their numerical simulation periodically detached themselves from a persistent low-level updraft and drifted rearward through the storm. They speculated that the periodic formation of new cells might be either a gravity wave phenomenon or a microphysical phenomenon related to the rate of rain production. Fovell and Ogura (1988) suggested that the decay of an older cell results from the formation of a new cell that cut off the moisture supply to the older cell but did not explicitly describe the mechanism responsible for the formation of a new cell. Rotunno et al. (1988) attributed the periodicity in cell formation to new cells being forced by the rain-produced cold pool surging out from previously generated cells. More recently, Yang and Houze (1995a) noted that there were no pulsations in the strength of

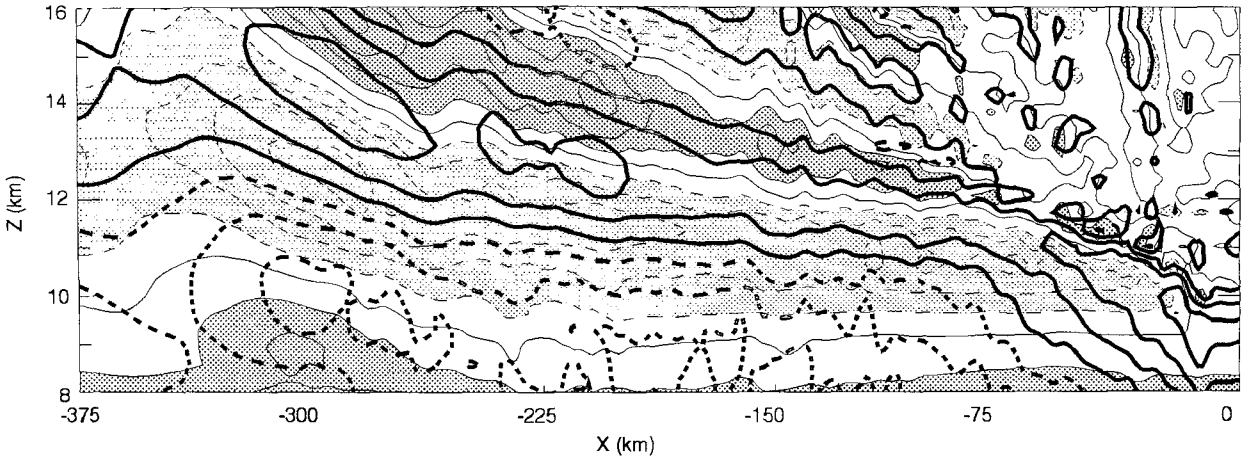

FIG. 14. Contours of potential temperature (thin lines, contoured as in Fig. 13) and horizontal velocity (thick lines, contoured in 5 m s^{-1} intervals) at $t = 6$ hours in the reference simulation. Light and dark shading indicate $\theta' < -2$ K and $\theta' > 2$ K, respectively.

the updraft at the leading edge of the cold pool, but cells formed by periodically detaching from the steady updraft. They showed that the amplitude and vertical structure of the velocity perturbations associated with these cells could be successfully reproduced using a linear model in which the horizontal wavelength and phase speed of the cells, as well as the vertical profile of the latent heating, were specified using data from a nonlinear simulation. Yang and Houze concluded on the basis of this linear analysis and the polarization of the velocity and pressure fields in nonlinear simulations that the cells were resonant trapped gravity waves.

Figure 15a shows the vertical velocity that develops in the dry simulation, which is forced by the steady pattern of heating and cooling shown in Fig. 6a. The vertical velocity field (thin lines) exhibits structure on a much finer spatial scale than the applied thermal forcing (thick lines). Cells appear in the vertical velocity field that resemble the vertical velocity cells in multicell squall lines, although their evolution is more chaotic than that of the cells in the reference simulation or in observations of actual squall lines. Gallus and Johnson (1995a) also noted some tendency for cellularity in the vertical velocity field in their numerical simulations even when the thermal forcing was steady, but they did not explore the issue further. Figures 15b, 15c, and 15d show the vertical velocity generated when the thermal forcing is reduced in magnitude. The cells vanish when the amplitude of the thermal forcing is reduced by a factor of 10 (Fig. 15c), but some cellularity remains when the thermal forcing is reduced in amplitude by a factor of 5 (Fig. 15b). When the thermal forcing has infinitesimal amplitude, so that the linear approximation is valid (Fig. 15d), the vertical velocity field is smooth and noncellular. The vertical velocity shown in Fig. 15d was computed using a fully linear model that is discussed in appendix A.

The simulations shown in Fig. 15 demonstrate that steady thermal forcing, with a magnitude characteristic of that present in the low-frequency components of actual squall lines, is sufficient to generate cellular updrafts in nonlinear simulations. No temporal variations in the forcing are required to produce these cells; instead, vertical velocity cells are an inevitable nonlinear consequence of a steady thermal forcing of sufficient magnitude. In actual squall lines, this unsmooth and unsteady response to the steady thermal forcing may excite the resonant gravity waves modes associated with the rearward cell propagation identified by Yang and Houze (1995a).

6. Are the wave dynamics linear?

If much of the mesoscale structure associated with squall lines is determined by gravity waves forced by the low-frequency component of the latent heating and cooling at the system's leading edge, one might ask to what extent these gravity waves can be described by linear dynamics. In order to investigate this question, a linear model (described in appendix A) was used to simulate the response of a Boussinesq atmosphere to the same thermal forcing used in the dry simulation. The linear model was integrated with no microphysical parameterization, the mean-state stability and horizontal winds were identical to those in the dry simulation shown in Fig. 4, and the thermal forcing was that shown in Fig. 6a.

The total horizontal velocity ($\bar{U} + u'$) that develops in the linear simulation is shown in Fig. 16, which can be compared to the corresponding nonlinear result shown in Fig. 5b. At upper levels the linear solution agrees reasonably well with the nonlinear solution; above $z > 6$ km, a FTRF is visible for $x < -75$ km and a rear to front flow appears that is similar to the

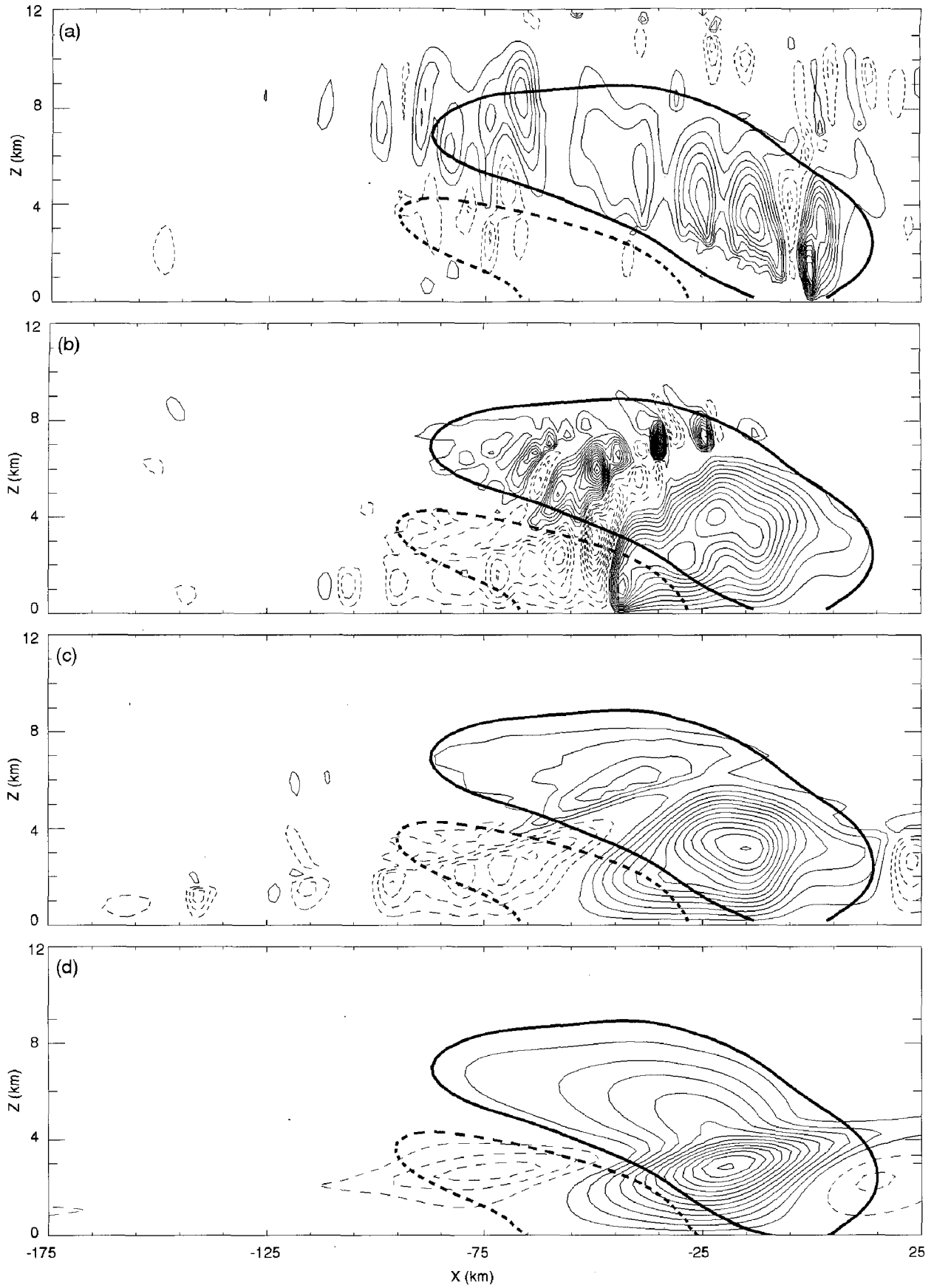
(a)
(b)
(c)
(d)
Z (km)
12
8
4
0
-175
-125
-75
-25
25
X (km)

LAF for $x > 0$ km. Below 6 km, however, the flow in the linear simulation differs dramatically from the nonlinear result. There is some indication of a RI in the linear solution, but it does not descend toward the gust front in a realistic manner and the low-level outflow behind the gust front is completely absent in the linear solution.

In an attempt to determine why the linear model failed to adequately reproduce the flow below $z = 6$ km, an additional linear simulation was conducted with the basic state modified so that the temperatures below $z = 1.5$ km matched those in the low-level cold pool that formed in the dry simulation. As in the previous simulation, the basic state remained horizontally uniform. This second linear simulation, shown in Fig. 17, did a far better job than the previous linear simulation of reproducing the rear inflow jet and other low-level features of the squall line to the rear of the thermal forcing. (Note that the basic state was not modified to incorporate information about the rear inflow jet; the only modification was to include a low-level cold pool.) Thus, it appears that the linear model fails to accurately represent the low-level circulations because it cannot account for the local modification of the basic-state stability associated with the development of the low-level cold pool.

7. Convective versus stratiform thermal forcing

Houze (1982) and Johnson and Young (1983) analyzed the vertical distribution of heating for the entire leading line–trailing anvil system. Houze (1982) noted that large-scale upward motion must occur to balance the upper-level heating. Gallus and Johnson (1992) concluded that latent heat absorption and release in the trailing anvil leads to the formation of a midlevel mesolow that is sufficiently strong to drive the RI. Yang and Houze (1995b) have concluded that the addition of a bulk-ice microphysical parameterization to a warm rain cloud model leads to a more realistic RI and asserted that the descending nature of the RI is a result of latent cooling associated with evaporation and sublimation within the trailing stratiform region. Zhang and Gao (1989) also pointed out the importance of melting and evaporative cooling in the stratiform region in producing a descending RI. The extent to which in situ microphysical forcing dominates the overall dynamics in the trailing anvil has, however, remained an open question. Recently, Gallus and Johnson (1995a,b) performed a series of simulations of the stratiform region of the 10–11 June 1985 squall line in which they specified one-dimensional profiles of thermal forcing and hydrometeor advection meant to represent inputs from the convective region at the lateral boundary of a 2D kinematic cloud model. They concluded that ice processes within the stratiform region were an important dynamical contribution to the circulation that developed in their model of the stratiform region.

On the other hand, many previous numerical and observational studies have specifically attributed the development of the RI to dynamical forcing from within the convective line (Smull and Houze 1987b; Lafore and Moncrieff 1989; Weisman 1992; Klimowski 1994). An additional dry simulation was, therefore, performed with the modified thermal forcing shown in Fig. 18a in order to investigate the relative importance of the stratiform and convective heating. Although there is no completely satisfactory procedure for splitting the total thermal forcing into convective and stratiform components, an attempt was made as follows. The instantaneous latent heating and cooling from time 4.5 to 6.5 hours in the reference simulation was averaged, and any heating or cooling rearward of $x = -50$ km was neglected in order to isolate the convective elements of the leading line. The resulting field was then smoothed and scaled in the same way as the thermal forcing used in the original dry simulation. This smoothing smears the thermal forcing slightly ahead of $x = 0$ km and rearward of $x = -50$ km.

The thermal forcing in Fig. 18a consists of a heating region that slants backward over a low-level cooling formed by the evaporation of precipitation. Although the 50-km-wide scale of the thermal forcing is clearly wider than an individual convective element, updrafts exceeding 3 m s^{-1} were visible in the reference simulation throughout this entire 50-km-wide region. This is roughly consistent with the analysis of Smull and Houze (1987a), who found an approximately 40-km-wide convective region in their observational study of the 22 May 1976 squall line (see their Fig. 3). Note also that the quasi-horizontal pattern of heating overlying cooling apparent in the region $x < -60$ km of the thermal forcing used in the dry simulation (Fig. 6a) has been eliminated from the thermal forcing shown in Fig. 18a.

The response to the thermal forcing shown in Fig. 18a is shown in Fig. 18b and can be compared to the response in the dry simulation, shown in Fig. 5b. The overall qualitative structure of the flow is similar in the two figures; the thermal forcing from the leading convective line is sufficient to generate the FTRF, the RI, and the LAF. The amplitudes of the FTRF, RI, and

FIG. 15. Vertical velocity (thin lines) and thermal forcing (thick lines) in (a) the dry simulation, (b) a nonlinear simulation with thermal forcing reduced by a factor of 5, (c) a nonlinear simulation with thermal forcing reduced by a factor of 10, and (d) a linear simulation with the thermal forcing as in (a). Contour interval on w is 0.5 m s^{-1} in (a), 0.1 m s^{-1} in (b), 0.05 m s^{-1} in (c), and 0.5 m s^{-1} in (d). Contours of the thermal forcing are ± 0.001 in (a), ± 0.0005 in (b), ± 0.0001 in (c), and ± 0.001 in (d).

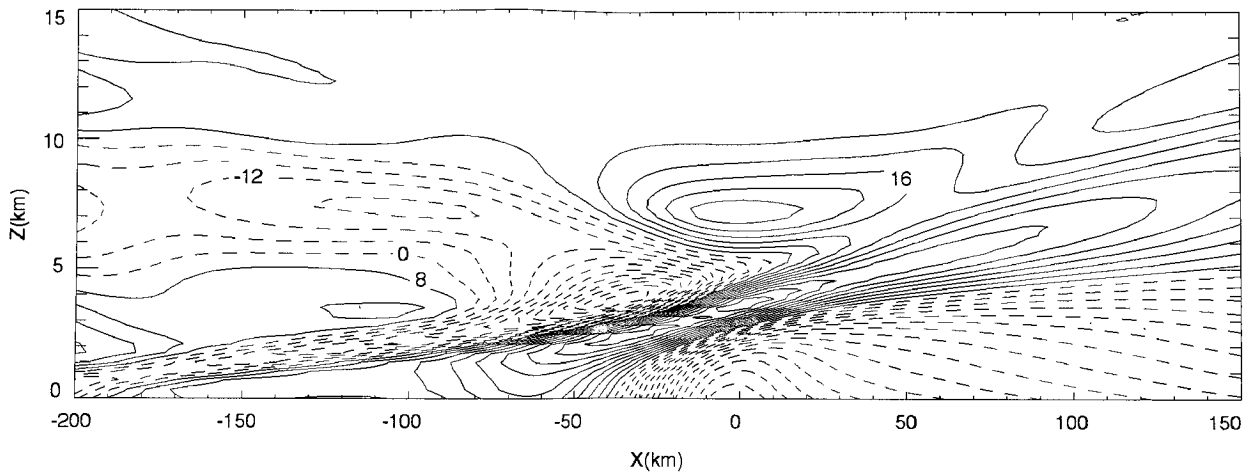

FIG. 16. Horizontal velocity (contoured in 4 m s^{-1} intervals) generated by the thermal forcing shown in Fig. 6a at time t = 3 h in a linear simulation.

LAF are smaller than in the dry simulation, indicating that thermal forcing in the stratiform region does augment and modify the stratiform circulation. This is consistent with the results of Yang and Houze (1995b), Zhang and Gao (1989), and Gallus and Johnson (1992, 1995a,b), who suggested that local microphysical processes can influence the trailing anvil circulation. In particular, in both dry simulations (Figs. 18b and 5b), the RI does not descend to the surface until it nearly reaches the gust front, whereas in the reference simulation (Fig. 5a) the RI descends over its entire 200-km length. This suggests that the realistic descent of the RI may depend on latent heating and cooling in the stratiform region that is so weak it fell below the threshold for inclusion in the thermal forcings used in the two dry simulations. Nevertheless, these results suggest that the thermal forcing from the leading convective line provides the primary forcing for the RI, FTRF, and LAF.

8. Sensitivity studies

The results of the previous sections demonstrate that gravity waves forced by the time-average pattern of latent heating and cooling in and near the leading convective line can generate the basic structures in the trailing stratiform anvil. The gravity waves themselves are influenced by both the environment through which they propagate and the pattern of latent heating and cooling that forces them. Additional numerical simu-

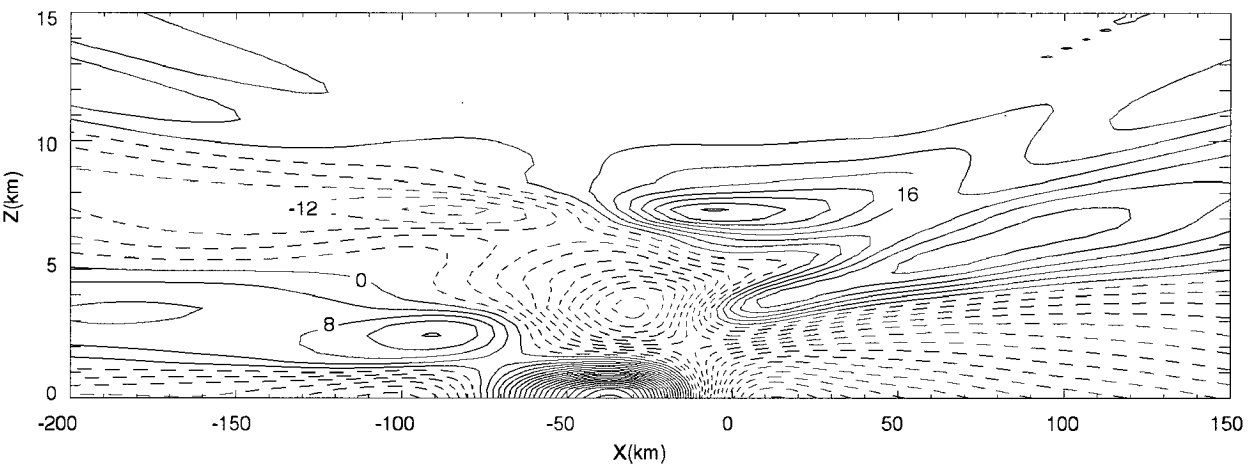

FIG. 17. Horizontal velocity field (contoured in 4 m s^{-1} intervals) generated by the thermal forcing shown in Fig. 6a at time t = 3 h in a linear simulation with modified low-level stability.

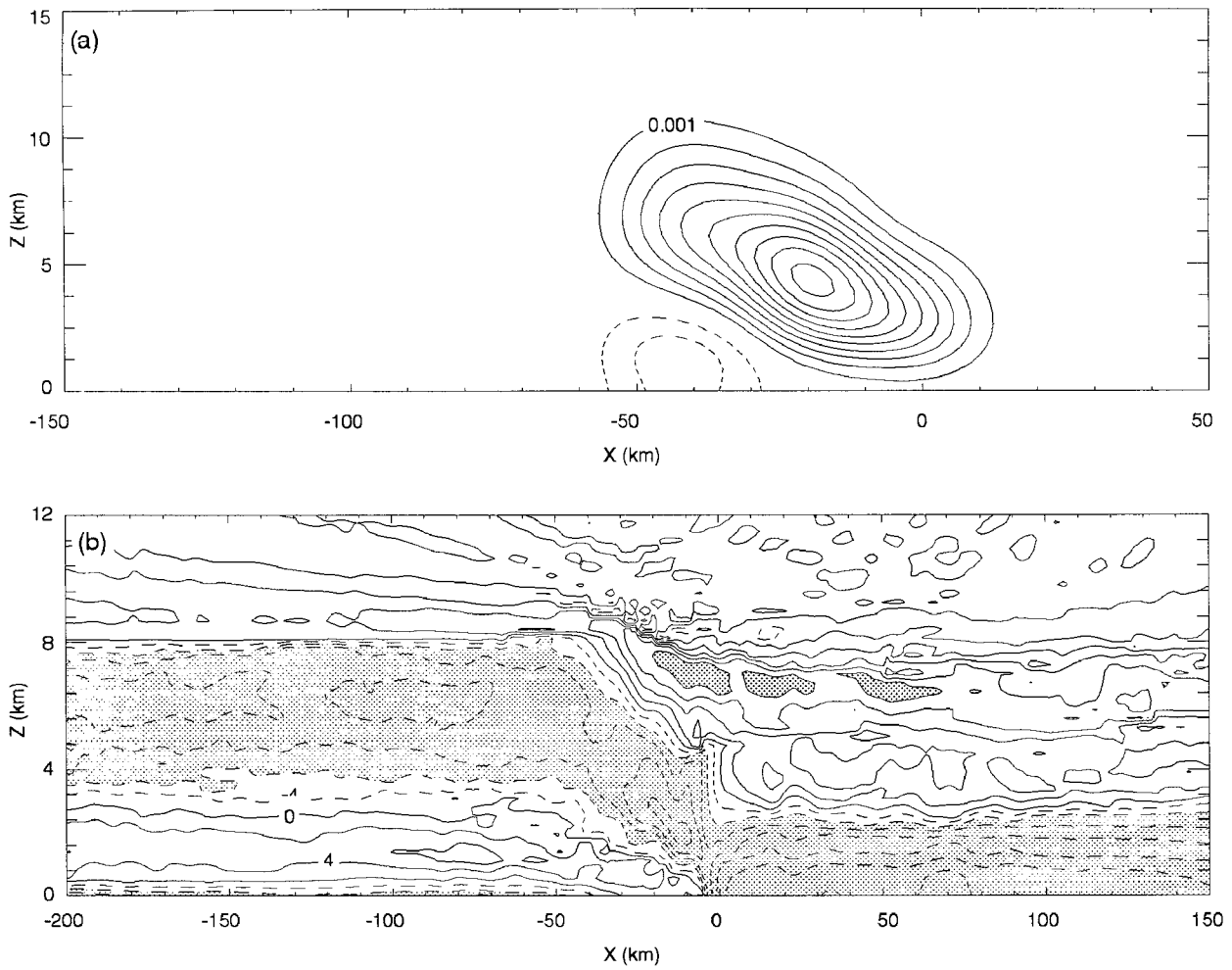

FIG. 18. (a) Time-mean thermal forcing meant to represent the forcing from the leading convective line alone (contours as in Fig. 6a). (b) Horizontal velocity at time $t = 6$ h generated by the thermal forcing in (a). Horizontal velocity contours and shading are as in Fig. 5. Note the difference in horizontal scale in Figs. 6a and 6b.

lations were performed in order to investigate the sensitivity of the mesoscale storm structure to changes in the large-scale environment and the thermal forcing. The large-scale environment and the applied thermal forcing were varied independently in these sensitivity studies. It should be noted, however, that in real squall lines, changes in the large-scale environment can influence the latent heating and cooling of the convective line. For example, Rotunno et al. (1988) have discussed how the environmental wind shear and CAPE affect the orientation of the updraft at the leading edge of the gust front and thereby influence the distribution of the thermal forcing. The following section should, therefore, be understood to examine only one aspect of the sensitivity of the squall line to the environment, namely the extent to which a hypothetical fixed thermal forcing would generate different mesoscale circulations within different environments.

a. Sensitivity to the environment

Figure 19 illustrates the influence of variations in the large-scale environment on the horizontal velocity field generated by the thermal forcing shown in Fig. 6a. In Fig. 19b the initial profile of the horizontal wind was the same as in the dry simulation, but the initial thermodynamic profile was modified so that the Brunt–Väisälä frequency was 0.01 s^{-1} below 2 km. This modification eliminates the well-mixed layer of constant $\overline{\theta}$ near the surface. The flow behind the thermal forcing in Fig. 19b looks very similar to the flow in the dry simulation (shown in Fig. 19a) except at low levels where the increased stability seems to weaken the flow (compare, for example, the RI in the two figures). Gallus and Johnson (1995b) found a similar decrease in the magnitude of the flow when they increased the initial stability in their numerical simulations of the strat-

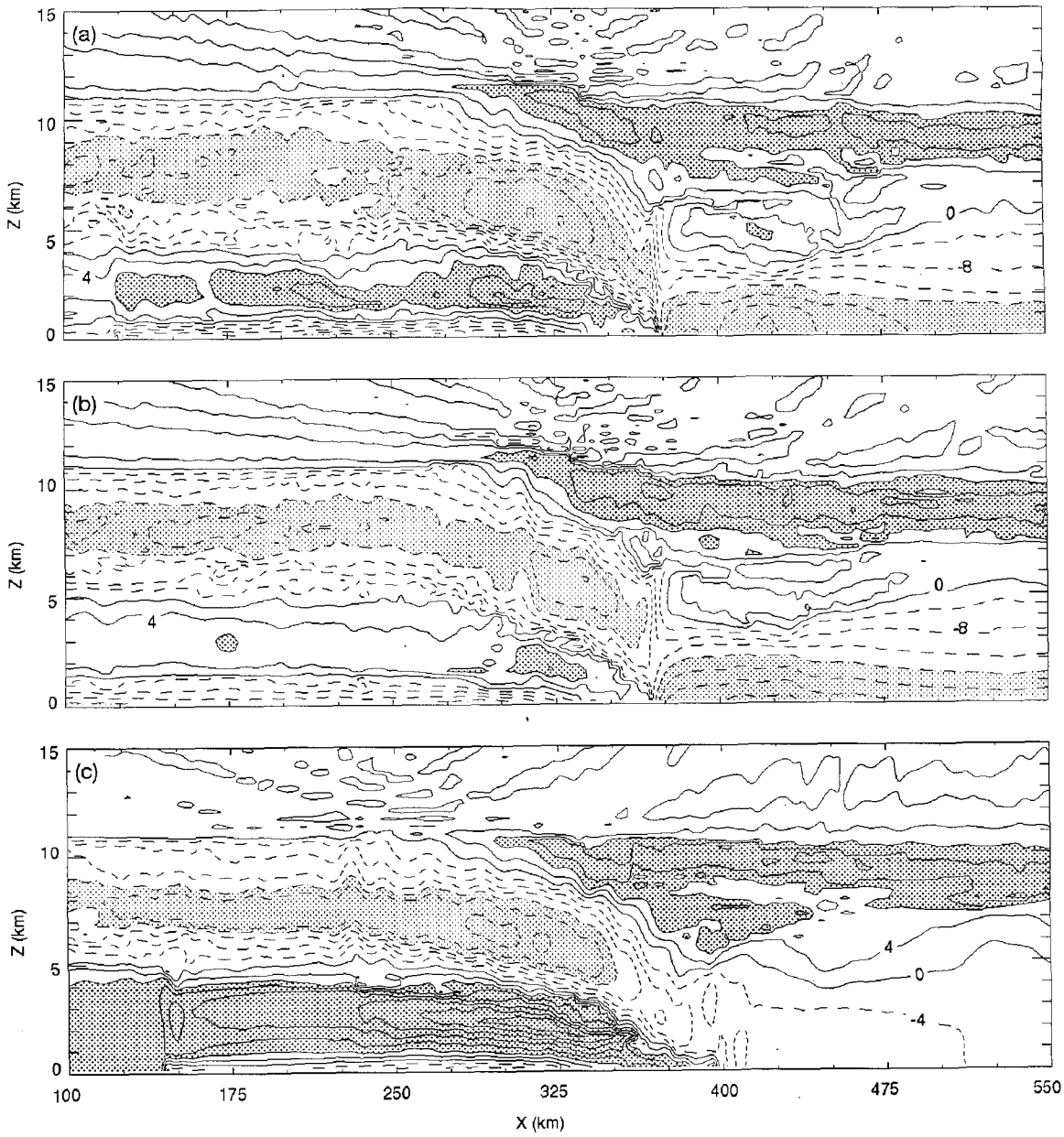

FIG. 19. Horizontal flow at time $t = 6$ h arising from the thermal forcing shown in Fig. 6a in (a) the dry simulation, (b) a simulation with modified low-level Brunt–Väisälä frequency, and (c) a simulation with modified low-level winds. Contours and shading are as in Fig. 5.

iform region of the 10–11 June squall line. Ahead of the thermal forcing, the LAF is slightly stronger in Fig. 19b. An additional simulation was performed with the initial Brunt–Väisälä frequency given by $N = 0.01\ s^{-1}$ throughout the entire depth of the model domain in order to examine the effect of variations in the upper-level stability. The flow that developed was very similar to the flow in Fig. 19b, suggesting that changing the upper-level stability does not strongly affect the circulation. Further, since the assumption of uniform Brunt–Väisälä frequency precludes the accurate representation of a tropopause, the similarity of the $N = 0.01\ s^{-1}$ experiment to that shown in Fig. 19b implies that the vertical extent of the circulation generated by the thermal forcing is not limited by the tropopause. This result will be explored in more detail in section 8c.

In Fig. 19c, the initial stability is the same as in the dry simulation, but the low-level shear in the initial wind was removed, setting $\bar{U} = 1\ m\ s^{-1}$ at all heights.

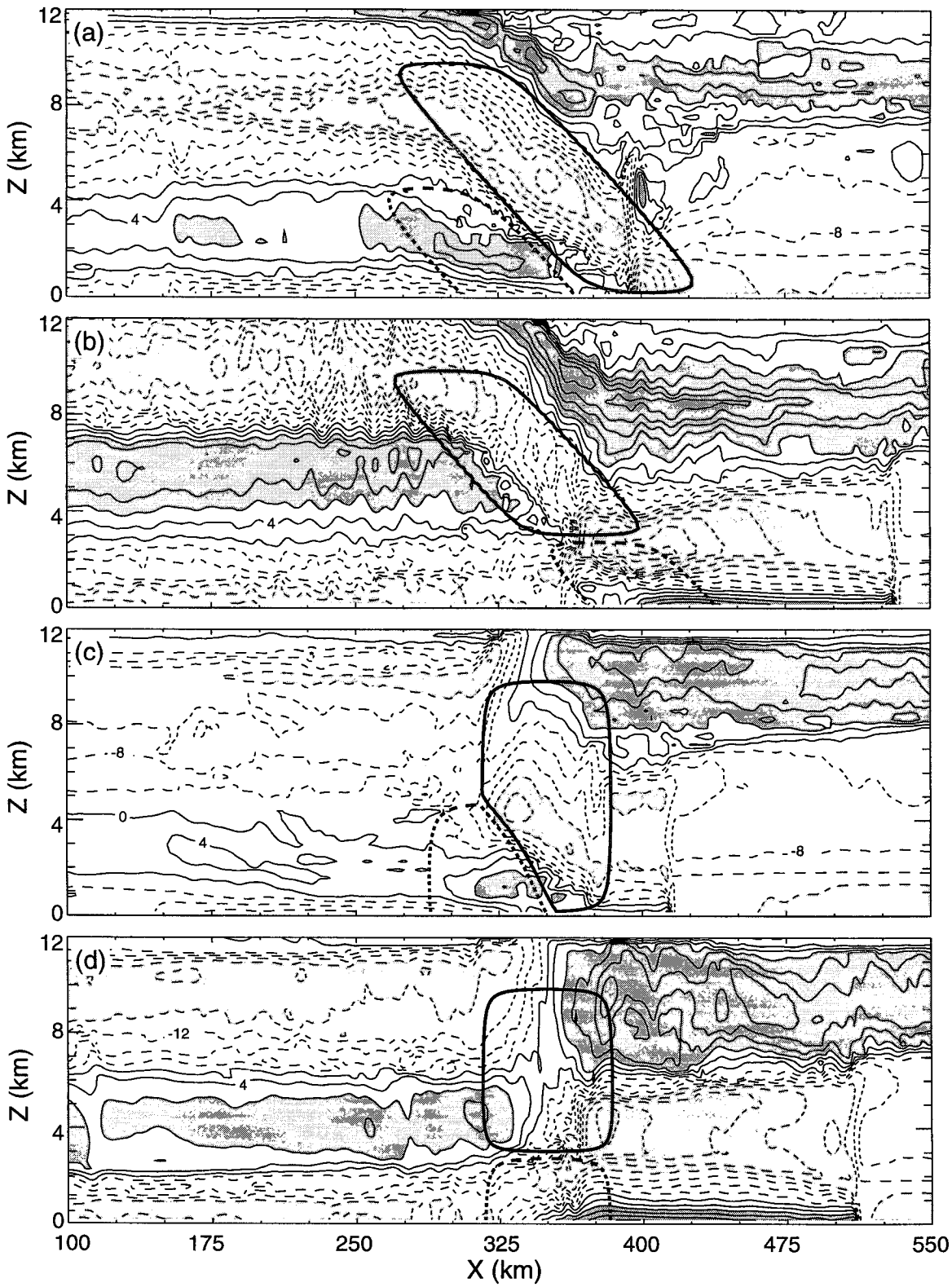

FIG. 20. Horizontal perturbation velocity (thin lines) generated by four distinct patterns of thermal forcing (thick lines) at time t = 6 h. Horizontal velocity contours and shading are as in Fig. 5. Thermal forcing contours are ± 0.001 K s^{-1}.

The flow in Fig. 19c is comparable to the flow in the dry simulation, shown in Fig. 19a, except in the lowest levels where the lack of an opposing wind exaggerates the strength of the RI and creates a gust front that runs out ahead of the storm. The difference in the low-level velocities in Figs. 19a and 19c is, in fact, comparable to the difference in the mean wind between the two simulations.

b. Sensitivity to the thermal forcing

In order to examine the sensitivity to the thermal forcing in a systematic way, an easily varied analytic thermal forcing was developed. (This forcing is described in appendix B.) Figure 20a shows the horizontal flow (thin lines) at time $t = 6$ h generated by this thermal forcing (thick lines). Like the thermal forcing shown in Fig. 6a, the thermal forcing in Fig. 20a consisted of a backward slanting region of heating trailed by a more compact backward-slanting region of cooling. Note that the flow in Fig. 20a resembles the circulation in a squall line.

Figure 20b shows the flow that resulted when the thermal forcing was modified so that the region of cooling was aligned along the same sloping axis as the region of heating. The flow that developed from this thermal forcing is qualitatively different from the flow shown in Fig. 20a, especially at low levels. The RI in Fig. 20b never descends to the surface as it does in the more representative flow shown in Fig. 20a. Ahead of the thermal forcing, there is a low-level region of rear to front flow that is not present in the 22 May 1976 squall lines or in Fig. 20a. Above this, Fig. 20b shows that the LAF extends to lower altitudes than in Fig. 20a.

The thermal forcing used in the simulation shown in Fig. 20c was identical to the thermal forcing indicated in Fig. 20a, except for the removal of the backward tilt to the heating and cooling. The most striking feature of the flow in Fig. 20c is the lack of any organized or coherent FTRF. At lower levels to the rear of the forcing, there is a region of RI, but it is relatively weak. Unlike the flow in Fig. 20b, however, the RI does descend to the surface. The LAF is too strong and there is a shallow low-level rear to front flow ahead of the region of heating.

Finally, Fig. 20d shows the flow that resulted when the cooling underlied the heating and both features lacked a backward tilt. As in Fig. 20b, the flow in Fig. 20d has an elevated RI that never descends to the gust front. The upper-level front to rear flow is stronger and better organized than in Fig. 20c, but the low-level rear to front flow is excessive and the upper-level LAF extends too low. Finally, the upper-level FTRF to the rear of the thermal forcing never connects to the flow ahead of the heating as it does in the 22 May 1976 squall line and in the flows in Figs. 20a, 20b, and 20c.

A circulation including a FTRF, LAF, and RI like that observed in the 22 May 1976 squall line only develops when the applied heating and cooling has the pattern shown by the heavy lines in Fig. 20a, suggesting that the mesoscale circulation is strongly influenced by the shape and structure of the applied thermal forcing. In contrast, the circulation in the mesoscale region surrounding the squall line shows much less sensitivity to variations in the mean-state environment. Figures 19a–c show that varying the mean-state stability and winds alone, while leaving the thermal forcing unchanged, varies the strength of the FTRF, LAF, and RI but does not fundamentally change the qualitative pattern of the mesoscale circulation. In real squall lines, however, changing the mean state environment may alter the distribution of latent heating and cooling within the region of the leading line. Given the results of these sensitivity studies, it appears that changes in the mean state environment will primarily influence the mesoscale circulation by changing the thermal forcing, rather than by affecting the propagation of low-frequency gravity waves generated by the thermal forcing.

Gallus and Johnson (1995a,b) reported that thermal forcing from the convective line alone did not generate a realistic circulation in the stratiform region. The apparent contradiction between their conclusions and our results can be reconciled on the basis of the sensitivity tests discussed here. As mentioned earlier, Gallus and Johnson modeled only the trailing anvil and specified a profile of heating and cooling along the upstream boundary to represent the thermal forcing from the convective line. The vertical profile of their specified heating and cooling was based on a heat budget derived from observations of a squall line (see Fig. 2b in Gallus and Johnson 1995b). Given the sensitivity of the circulations in the stratiform region to small changes in the thermal forcing, their vertical, one-dimensional profile of heating and cooling may not have been sufficient to generate a realistic flow in the trailing stratiform anvil.

c. The vertical extent of the anvil cloud

It was noted in section 8a that removing the tropopause had almost no effect on the vertical extent of the mesoscale circulation generated by thermal forcing, which suggests that the height of the top of anvil cloud might be relatively insensitive to the height of the tropopause. This hypothesis can be tested by comparing two microphysical squall line simulations: one with and one without a tropopause.

The initial potential temperature profile used in these simulations was adapted from the widely used idealized midlatitude sounding of Weisman and Klemp (1982), such that

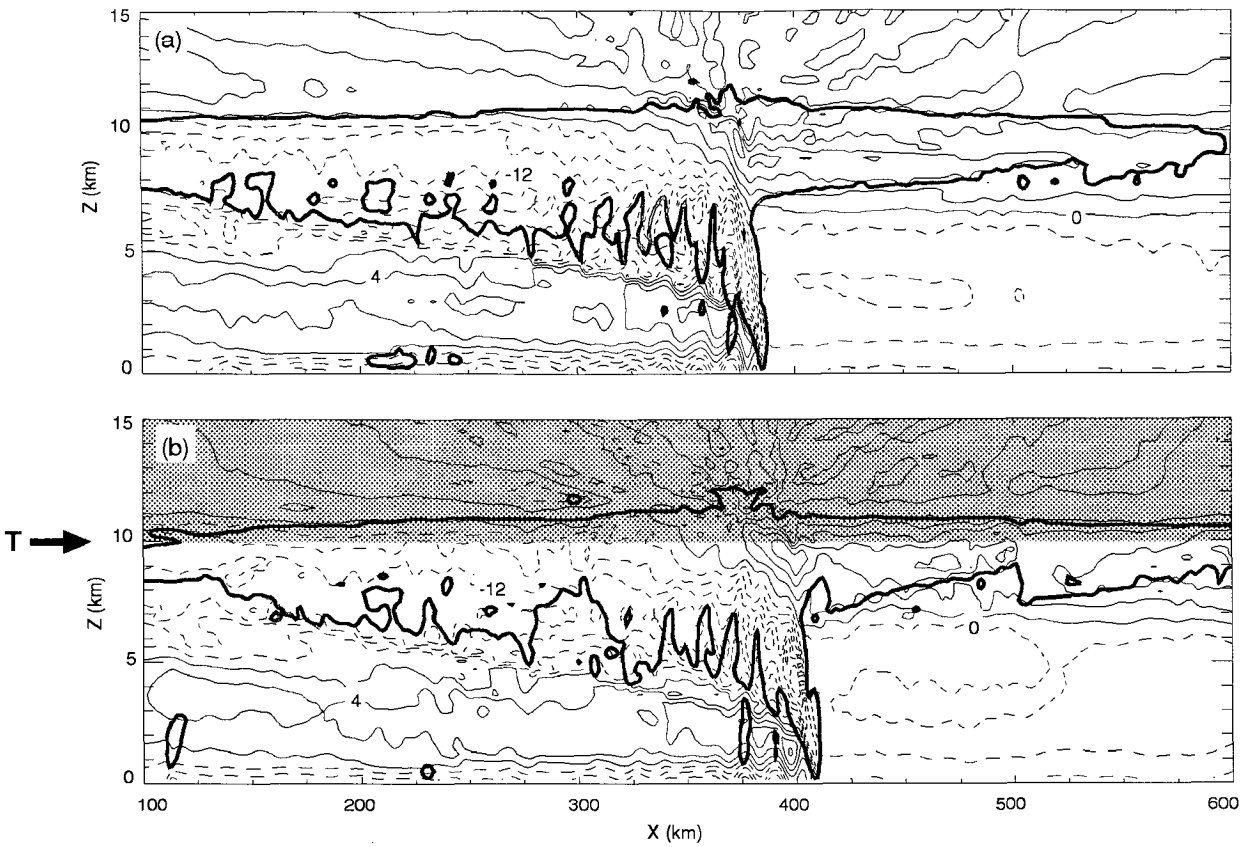

FIG. 21. Horizontal velocity (thin lines, contoured in 4 m s^{-1} intervals) and cloud outline (thick lines) in "moist" simulations in an environment: (a) with no tropopause and (b) a tropopause at z = 10 km. Shading in (b) indicates the stratosphere.

$$\bar{\theta}(z) = \begin{cases} \theta_0 + (343\ \text{K} - \theta_0)\left(\dfrac{z}{12\ \text{km}}\right)^{5/4} \\ \qquad\qquad \text{if} \quad z \leq z_{tr} \\ \left[\left(\dfrac{z_{tr}}{12\ \text{km}}\right)^{5/4} - 1\right](343 - \theta_0) \\ \quad + 343\ \text{K} \exp\left[\dfrac{g}{c_p 243\ \text{K}}(z - z_{tr})\right] \\ \qquad\qquad z > z_{tr}, \end{cases} \tag{7}$$

where z_{tr} indicates the height of the tropopause and θ_0 is the potential temperature at the surface. The initial profile of relative humidity was as given in Weisman and Klemp (1982), and the mixing ratio was not allowed to exceed 0.016 at low levels. The initial profile of the winds was also based on profiles used in Weisman and Klemp (1982) and is given by

$$\bar{U} = U_0\left[\tanh\left(\frac{z}{z_u}\right) - 1\right], \tag{8}$$

where U_0 = 12 m s^{-1} and z_u = 3 km.

Figure 21a shows the horizontal velocity (thin lines) and cloud outline (thick lines) at a time t = 6 into the simulation of a storm where the tropopause was eliminated by setting $z_{tr} = \infty$ in (7). The horizontal velocity field shows all the expected features of a squall line and the mesoscale cloud top is fairly uniform at $z \sim 11$ km except in the overshooting cloud tops of the region of active convection ($x \sim 390$ km). Figure 21b shows the flow and cloud outline in a simulation with the height of the tropopause set to 10 km. The presence of the stratosphere in this second simulation has very little effect on the squall line. In particular, the top of the anvil cloud is again found at approximately 11 km. Recall that the vertical extent of the quasi-horizontal disturbances generated by the idealized small-amplitude heating profiles shown in Figs. 2 and 10 are determined exclusively by the depth of the thermal forcing. It appears that the depth of the thermal forcing is also the primary factor determining the height of the anvil cloud in these moist simulations. As indicated by the height of the overshooting cloud tops in Figs. 21a and 21b, the depth of the main convective towers in the leading line is similar in both simulations, and, according to the preceding hypothesis, there should be

little change in the elevation of the top of the anvil cloud. Moreover, when the depth of the convective towers was reduced in an additional simulation (not shown) in which the tropopause was lowered to 8 km, the top of the anvil cloud descended to 9 km. Even in this last case, however, the anvil cloud penetrated the stratosphere. Thus, the height of the top of the anvil cloud appears to be primarily determined by the depth of the convection in the leading line. The tropopause influences the height of the anvil only indirectly by limiting the depth of the convection in situations where the tropopause is located well below the level at which air parcels in the main updraft cores return to a state of neutral buoyancy.

Note that the mesoscale cloud top in Fig. 21b lies above the tropopause, suggesting that a large area of cloudiness can occur within the stratosphere. Although this storm is a simulated one, the real occurrence of such a system might be important in understanding the exchange of water vapor across the tropopause.

9. Conclusions

The division between the leading convective line and the trailing stratiform region of a squall line system has generally been made on the basis of the difference between the precipitation and radar echo signatures in each region. The results presented in this paper suggest the two regions may also be differentiated on the basis of the role played by buoyancy forces in the dynamical processes operating in each region. Motion in the convective region is dominated by positively and negatively buoyant plumes of rising and sinking air. On the other hand, buoyancy acts primarily as a restoring force in the trailing stratiform region and in the larger mesoscale environment surrounding the cloud. The perturbations that form in the stratiform regions are primarily gravity waves forced by the low-frequency components of the latent heat released and absorbed in the leading convective line. The velocity perturbations in these finite-amplitude waves play a major role in determining the shape of the stratiform anvil by advecting parcels of cloudy air laterally away from the convective updrafts in the leading line.

The role of gravity waves was demonstrated by comparing a moist simulation of a two-dimensional squall line with a trailing stratiform anvil obtained with a conventional cloud model to a dry simulation driven by steady thermal forcing. This steady forcing was obtained by spatially smoothing and temporally averaging the field of latent heating and cooling released in and just behind the convective leading line during the mature phase of the squall line in the moist simulation. The dry simulation reproduced the major dynamical features that occur in the mesoscale region around the leading line, including the ascending front to rear flow (FTRF), the rear inflow jet (RI), the flow in the leading anvil (LAF), the mesoscale updrafts and downdrafts in the stratiform region, and the upper-level cold anomaly near the top of the stratiform anvil cloud. In addition, the upper-level advection of diabatically lifted air by the perturbed horizontal flow in the dry simulation resulted in a pattern of vertically displaced air that strongly resembled the leading and trailing stratiform clouds in the reference simulation. Even the cellular character of the individual updrafts and downdrafts was crudely reproduced in the dry simulation, in spite of the fact that the thermal forcing was steady with time. The quasi-steady cellular response to the thermal forcing arose as a consequence of the nonlinear flow dynamics and disappeared in additional simulations in which the amplitude of the thermal forcing was decreased.

An additional numerical simulation, in which the thermal forcing was limited to that produced in the leading convective line, revealed that the thermal forcing from the leading convective line alone is sufficient to generate a qualitatively correct mesoscale circulation, including an RI, FTRF, and LAF. This suggests that, although local thermal forcing in the stratiform region may modify the circulation around squall lines, the mesoscale circulation around squall lines is determined primarily by the distribution of the thermal forcing from the leading convective line.

The extent to which the wave dynamics in the stratiform region are governed by linear theory was investigated by repeating the dry simulation using a linear model. The linear model did a reasonable job of reproducing the upper-tropospheric perturbations in the nonlinear moist and dry simulations but the linear solution for lower-tropospheric flow was not even qualitatively correct. A serious defect in the linear solution was shown to result from its failure to account for the nonlinear modification of the basic state that develops after the formation of the low-level cold pool.

According to the preceding results, one might expect the mesoscale circulation around the squall line to be determined by the distribution of the thermal forcing within the region of the leading convective line and by the wave-propagation characteristics of the mesoscale environment surrounding the convective region. The wave propagation characteristics of the environment are governed by the vertical profiles of static stability and horizontal wind speed. A series of dry simulations, in which the thermal forcing was held constant, demonstrated that the mesoscale circulation was relatively insensitive to changes in the wave-propagation characteristics in the environment containing the leading line. A second series of dry simulations, in which the mesoscale environment was held fixed, showed great sensitivity to variations in the shape of the thermal forcing. In particular, realistic mesoscale circulations did not develop without a backward slant to the zone of maximum heating and a rearward displacement of the low-level cooling with respect to the low-level heating.

The distribution of the latent heating within the convective region is not actually independent of the wave-

propagation characteristics in the environment surrounding the squall line. As demonstrated by Rotunno et al. (1988), the vorticity balance at the gust front plays a crucial role in determining the orientation of individual convective cells and thereby influences the distribution of the thermal forcing in the convective region. This vorticity balance is dependent upon many of the same factors that govern wave propagation in the surrounding environment, including the low-level wind shear and the low-level stability. Given the strong sensitivity of the squall line to variations in the thermal forcing, any changes in a squall line's low-level environment would be likely to influence the structure of the stratiform region through changes in the thermal forcing, rather than through changes in the propagation of the gravity waves themselves.

The sensitivity of the stratiform region to the heating in the leading convective line was underscored by a series of moist simulations demonstrating the relative insensitivity of the height of anvil cloud to the location of the tropopause. These simulations suggest that the height of the anvil cloud is primarily determined by the depth of the thermal forcing in the leading convective line. The depth of this thermal forcing may also be sensitive to the height of the tropopause since a sufficient lowering of the tropopause will lower the equilibrium level at which rising air parcels become neutrally buoyant. Nevertheless, if the convection in the leading line is sufficiently deep, the entire top of the anvil cloud can penetrate into the stratosphere.

Acknowledgments. This research was supported by the National Science Foundation Grant ATM-9218376. In addition, Rajul Pandya was supported by a NSF Graduate Fellowship. Computer resources were provided by the National Center for Atmospheric Research, which is sponsored by the National Science Foundation. The authors would like to thank Drs. Robert Houze and Brad Smull for helpful discussions, as well as Drs. Brian Mapes and J. M. Fritsch for their comments that helped to improve the manuscript.

APPENDIX A

A Linear Model

In order to investigate the role of linearity in the mesoscale circulations around squall lines, a numerical model was developed to integrate the linear Boussinesq equations. In a horizontally uniform basic state with a mean wind of $\bar{U}$ and stability N, the set of two-dimensional incompressible Boussinesq equations are

$$\left(\frac{\partial}{\partial t} + \bar{U}\frac{\partial}{\partial x}\right)u' + w\frac{\partial \bar{U}}{\partial z} + \frac{1}{\rho_0}\frac{\partial p'}{\partial x} = 0$$

$$\left(\frac{\partial}{\partial t} + \bar{U}\frac{\partial}{\partial x}\right)w' + \frac{1}{\rho_0}\frac{\partial p'}{\partial z} = b$$

$$\left(\frac{\partial}{\partial t} + \bar{U}\frac{\partial}{\partial x}\right)b + w'N^2 = Q$$

$$\frac{\partial u'}{\partial x} + \frac{\partial w'}{\partial z} = 0,$$

where Q represents the thermal forcing, u' is the perturbation horizontal wind, w' is the perturbation vertical velocity, and b is the buoyancy. These equations can be combined to give

$$\left(\frac{\partial}{\partial t} + \bar{U}\frac{\partial}{\partial x}\right)^2\left(\frac{\partial^2 w'}{\partial z^2} + \frac{\partial^2 w'}{\partial x^2}\right) - \frac{\partial^2 \bar{U}}{\partial z^2}\left(\frac{\partial^2 w'}{\partial x \partial t} + \bar{U}\frac{\partial^2 w'}{\partial x^2}\right) + N^2\frac{\partial^2 w'}{\partial x^2} = \frac{\partial^2 Q}{\partial x^2}. \quad \text{(A1)}$$

Equation (A1) was solved by first horizontally transforming to spectral space, giving

$$\left(-\frac{\partial^2}{\partial t^2} - 2ik\bar{U}\frac{\partial}{\partial t} + \bar{U}^2k^2\right)\left(\frac{\partial^2 \hat{w}}{\partial z^2} - k^2\hat{w}\right) + \frac{\partial^2 \bar{U}}{\partial z^2}\left(ik\frac{\partial \hat{w}}{\partial t} - \bar{U}k^2\hat{w}\right) + N^2k^2\hat{w} = k^2\hat{Q}, \quad \text{(A2)}$$

where the $\hat{w}$ is the horizontal Fourier transform of w' and k is the horizontal wavelength. The numerical integration of (A2) is done by first approximating (A2) by the finite-difference equation

$$\delta_t^2\delta_z^2\hat{w} + 2\bar{U}ik\delta_{2t}\delta_z^2\hat{w} - k^2\delta_t^2\hat{w} - 2\bar{U}ik^3\delta_{2t}\hat{w} - ik\frac{\partial^2 \bar{U}}{\partial z^2}\delta_{2t}\hat{w} = +\bar{U}^2k^2\left(\frac{\partial^2 \hat{w}}{\partial z^2} - k^2\hat{w}\right) - \left\langle \bar{U}k^2\frac{\partial^2 \bar{U}}{\partial z^2}\hat{w}\right\rangle_t + N^2k^2\hat{w} - k^2\hat{Q}, \quad \text{(A3)}$$

where $\langle\ \rangle_t$ is an averaging operator defined such that

$$\langle f\rangle_t = [f(t + \Delta t) + f(t - \Delta t)]/2,$$

δ_{nz} is a finite-difference operator defined such that

$$\delta_{nz}f(z) = [f(z + n\Delta z/2) - f(z - n\Delta z/2)]/(n\Delta z),$$

and, from the definition of δ_{zx},

$$\delta_z^2 f = \delta_z(\delta_z f) = \frac{f(z + \Delta z) - 2f(z) + f(z - \Delta z)}{(\Delta z)^2}.$$

Expanding (A3) and grouping like terms gives an equation of the form

$$A\hat{w}_{m+1}^{n+1} + B\hat{w}_m^{n+1} + C\hat{w}_{m-1}^{n+1} = \mathcal{F}(\hat{w}_{m+1}^n, \hat{w}_m^n, \hat{w}_{m-1}^n, \hat{w}_{m+1}^{n-1}, \hat{w}_m^{n-1}, \hat{w}_{m-1}^{n-1}, \hat{Q}). \quad \text{(A4)}$$

The subscripts here refer to the vertical level [i.e., $\hat{w}_m = \hat{w}(m\Delta z)$, where Δz is the vertical grid spacing], while the superscripts refer to time. The upper boundary was treated using a radiation condition similar to that of Klemp and Durran (1983),

$$\left(\frac{\partial}{\partial t} + i\bar{U}k\right) = -|k|N\hat{w}, \qquad \text{(A5)}$$

which allows only upward propagating waves. This condition was applied to the uppermost point of the computational domain.

Combining (A5) and (A4) gives a closed tridiagonal matrix that can be inverted using standard techniques to find $\hat{w}$ at the $n + 1$ time level. A fast Fourier transform routine is then used to find w'. Open lateral boundaries were approximated by using a periodic horizontal domain. There is no need for any spatial smoothing since the linearity of this model precludes the possibility of nonlinear instability. The absence of an energy cascade to small scales means there is no need to parameterize subgrid-scale processes like eddy diffusion. Because of its linearity, the model can always be made to converge to a solution by the appropriate choice of grid spacing and step size.

APPENDIX B

Description of the Analytic Thermal Forcing

The analytic heat source used in the sensitivity studies described in section 8b is given by

$$Q(x, z) = Q_h q_x^h(\hat{x}_h) q_z^h(z - z_c) + Q_c q_x^c(\hat{x}_c) q_z^c(z - z_c), \qquad \text{(B1)}$$

where the first term represents the heating and the second the cooling. Values of Q_h were chosen for each of the four heating profiles discussed in section 8b so that the integrated heating matched the integrated heating of the thermal forcing shown in Fig. 6a. Values of Q_c were similarly chosen to scale the integrated cooling according to the integrated cooling in Fig. 6a. The spatial structure of the heating and cooling functions was specified by q_x^h, q_z^h, q_x^c, and q_z^c as follows:

$$q_x^h(\hat{x}_h) = \begin{cases} \cos\left[\dfrac{2\pi}{\lambda_{xh}}(\hat{x}_h)\right] & \text{if} \quad |\hat{x}_h| < \dfrac{\lambda_{zh}}{4} \\ 0 & \text{otherwise,} \end{cases}$$

$$q_z^h(z - z_h) = \begin{cases} \cos\left[\dfrac{2\pi}{\lambda_{zh}}(z - z_h)\right] & \text{if} \quad |z - z_h| < \dfrac{\lambda_{zh}}{4} \\ 0 & \text{otherwise,} \end{cases}$$

$$q_x^c(\hat{x}_c) = \begin{cases} \cos\left[\dfrac{2\pi}{\lambda_{xc}}(\hat{x}_c)\right] & \text{if} \quad |\hat{x}_c| < \dfrac{\lambda_{xc}}{4} \\ 0 & \text{otherwise,} \end{cases}$$

and

$$q_z^c(z - z_c) = \begin{cases} \cos\left[\dfrac{2\pi}{\lambda_{zc}}(z - z_c)\right] & \text{if} \quad |z - z_c| < \dfrac{\lambda_{zc}}{4} \\ 0 & \text{otherwise,} \end{cases}$$

where

$$\hat{x}_c = x - x_c + (z - z_c)\tan\theta,$$

$$\hat{x}_h = x - x_h + (z - z_h)\tan\theta.$$

For all the simulations presented in Fig. 20, $z_c = 1.5$ km, $x_h = 350$ km, $z_h = 5$ km, $\lambda_{xc} = 140$ km, $\lambda_{xh} = 140$ km, $\lambda_{zc} = 14$ km, and $\lambda_{zh} = 20$ km. In Fig. 20a, $x_c = 320$ km and $\theta = 85°$, while in Fig. 20b, $x_c = 390$ km and $\theta = 85°$. In Fig. 20c, $x_c = 320$ km and $\theta = 0°$, while in Fig. 20b, $x_c = 350$ km and $\theta = 0°$.

REFERENCES

Bougeault, P., 1983: A non-reflective upper boundary condition for limited-height hydrostatic models. *Mon. Wea. Rev.*, **111,** 420–429.

Bretherton, C., 1988: Group velocity and the linear response of stratified fluids to internal heat or mass sources. *J. Atmos. Sci.*, **45,** 81–93.

Cram, J. M., R. A. Pielke, and W. R. Cotton, 1992: Numerical simulations and analysis of a prefrontal squall line. Part II: Propagation of the squall line as an internal gravity wave. *J. Atmos. Sci.*, **49,** 209–225.

Davies, H. C., 1979: Phase-lagged wave-CISK. *Quart. J. Roy. Meteor. Soc.*, **105,** 325–353.

Dudhia, J., M. W. Moncrieff, and D. K. So, 1987: The two-dimensional dynamics of west African squall lines. *Quart. J. Roy. Meteor. Soc.*, **113,** 121–146.

Durran, D. R., and J. B. Klemp, 1982: On the effects of moisture on the Brunt–Väisälä frequency. *J. Atmos. Sci.*, **39,** 2152–2158.

——, and ——, 1983: A compressible model for the simulation of moist mountain waves. *Mon. Wea. Rev.*, **111,** 2341–2361.

——, M.-J. Yang, D. N. Slinn, and R. G. Brown, 1993: Toward more accurate wave-permeable boundary conditions. *Mon. Wea. Rev.*, **121,** 604–620.

Fovell, R., and Y. Ogura, 1988: Numerical simulation of a squall line in two dimensions. *J. Atmos. Sci.*, **45,** 3846–3879.

——, D. R. Durran, and J. R. Holton, 1992: Numerical simulations of convectively generated stratospheric gravity waves. *J. Atmos. Sci.*, **49,** 1427–1442.

Fritsch, J. M., and J. M. Brown, 1982: On the generation of the convectively driven mesohighs aloft. *Mon. Wea. Rev.*, **110,** 1554–1563.

Gallus, W. A., Jr., and R. H. Johnson, 1992: The momentum budget of an intense midlatitude squall line. *J. Atmos. Sci.*, **49,** 422–450.

——, and ——, 1995a: The dynamics of circulations within the trailing stratiform region of squall lines. Part I: The 10–11 June PRE-STORM system. *J. Atmos. Sci.*, **52,** 2161–2187.

——, and ——, 1995b: The dynamics of circulations within the trailing stratiform region of squall lines. Part II: Influence of the convective line and ambient environment. *J. Atmos. Sci.*, **52,** 2188–2211.

Gamache, J. F., and R. A. Houze Jr., 1985: Further analysis of the composite wind and thermodynamic structure of the 12 September GATE squall line. *Mon. Wea. Rev.*, **113,** 1241–1259.

Houze, R. A., Jr., 1977: Structure and dynamics of a tropical squall line. *Mon. Wea. Rev.*, **105,** 1540–1567.

——, 1982: Cloud clusters and large-scale vertical motions in the Tropics. *J. Meteor. Soc. Japan*, **60,** 396–409.

——, S. A. Rutlidge, M. I. Biggerstaff, and B. F. Smull, 1989: Interpretation of Doppler weather-radar displays in midlatitude mesoscale convective systems. *Bull. Amer. Meteor. Soc.*, **70,** 608–609.

Johnson, R. H., and G. S. Young, 1983: Heat and moisture budgets of tropical mesoscale anvil clouds. *J. Atmos. Sci.*, **40,** 2138–2146.

——, W. A. Gallus Jr., and M. D. Vescio, 1990: Near-tropopause vertical motion within the trailing stratiform region of a midlatitude squall line. *J. Atmos. Sci.*, **47,** 2200–2210.

Klemp, J. B., and R. B. Wilhelmson, 1978: The simulation of three-dimensional convective storm dynamics. *J. Atmos. Sci.*, **35,** 1070–1096.

——, and D. R. Durran, 1983: An upper boundary condition permitting internal gravity wave radiation in numerical mesoscale models. *Mon. Wea. Rev.*, **111,** 430–444.

Klimowski, B. A., 1994: Initiation and development of rear inflow within the 28–29 June 1989 North Dakota mesoconvective system. *Mon. Wea. Rev.*, **122,** 765–779.

Koch, S. E., R. E. Golus, and B. Dorian, 1988: A mesoscale gravity wave event observed during CCOPE. Part II: Interaction between the mesoscale convective systems and the antecedent waves. *Mon. Wea. Rev.*, **116,** 2545–2569.

Lafore, J.-P., and M. W. Moncrieff, 1989: A numerical investigation of the organization and interaction of the convective and stratiform regions of tropical squall lines. *J. Atmos. Sci.*, **46,** 521–544.

Ley, B. E., and W. R. Peltier, 1978: Wave generation and frontal collapse. *J. Atmos. Sci.*, **35,** 3–17.

Lindzen, R. S., 1974: Wave-CISK in the tropics. *J. Atmos. Sci.*, **31,** 156–179.

Mapes, B. E., 1993: Gregarious tropical convection, *J. Atmos. Sci.*, **50,** 2026–2037.

Miller, D. A., and F. Sanders, 1980: Mesoscale conditions for the severe conditions of 3 April 1974 in the east-central United States. *J. Atmos. Sci.*, **37,** 1041–1055.

Miller, P. P., and D. R. Durran, 1991: On the sensitivity of downslope windstorms to the asymmetry of the mountain profile. *J. Atmos. Sci.*, **48,** 1457–1473.

Nehrkorn, T., 1986: Wave-CISK in a baroclinic basic state. *J. Atmos. Sci.*, **43,** 2773–2791.

Nicholls, M. E., R. A. Pielke, and W. R. Cotton, 1991: Thermally forced gravity waves in an atmosphere at rest. *J. Atmos. Sci.*, **48,** 1869–1884.

Ogura, Y., and M.-T. Liou, 1980: The structure of a midlatitude squall line: A case study. *J. Atmos. Sci.*, **37,** 553–567.

Pandya, R., D. Durran, and C. Bretherton, 1993: Comments on "Thermally forced gravity waves in an atmosphere at rest.". *J. Atmos. Sci.*, **50,** 4098–4101.

Pearson, R. A., 1974: Consistent boundary conditions for numerical models of systems that admit dispersive waves, *J. Atmos. Sci.*, **31,** 1481–1489.

Raymond, D. J., 1976: Wave-CISK and convective meso-systems. *J. Atmos. Sci.*, **33,** 2392–2398.

——, 1984: A wave-CISK model of squall lines. *J. Atmos. Sci.*, **41,** 1946–1958.

Rotunno, R., J. B. Klemp, and M. L. Weisman, 1988: A theory for long-lived squall lines. *J. Atmos. Sci.*, **45,** 463–485.

Schmidt, J. M., and W. R. Cotton, 1990: Interactions between upper and lower tropospheric gravity waves on squall line structure and maintenance. *J. Atmos. Sci.*, **47,** 1205–1222.

Skamarock, W. C., and J. B. Klemp, 1992: The stability of time-split numerical methods for the hydrostatic and nonhydrostatic elastic equations. *Mon. Wea. Rev.*, **120,** 2109–2127.

Smull, B. F., and R. A. Houze Jr., 1985: A mid-latitude squall line with a trailing region of stratiform rain: Radar and satellite observations. *Mon. Wea. Rev.*, **113,** 117–133.

——, and ——, 1987a: Dual-Doppler analysis of a midlatitude squall line with a trailing region of stratiform rain. *J. Atmos. Sci.*, **44,** 2128–2148.

——, and ——, 1987b: Rear inflow in squall lines with trailing stratiform precipitation. *Mon. Wea. Rev.*, **115,** 2869–2889.

Uccellini, L. W., 1975: A case study of apparent gravity wave initiation of severe convective storms. *Mon. Wea. Rev.*, **103,** 497–513.

Weisman, M. L., and J. B. Klemp, 1982: The dependence of numerically simulated convective storms on vertical wind shear and buoyancy. *Mon. Wea. Rev.*, **110,** 504–520.

—— and ——, 1992: The role of convectively generated rear-inflow jets in the evolution of long-lived mesoconvective systems. *J. Atmos. Sci.*, **49,** 1826–1847.

Xu, Q., and J. H. E. Clark, 1984: Wave-CISK and mesoscale convective systems. *J. Atmos. Sci.*, **41,** 2089–2107.

Yang, M.-J., and R. A. Houze Jr., 1995a: Multicell squall line structure as a manifestation of vertically trapped gravity waves. *Mon. Wea. Rev.*, **123,** 643–661.

——, and ——, 1995b: Sensitivity of squall-line rear inflow to ice microphysics and environmental humidity. *Mon. Wea. Rev.*, **123,** 3175–3193.

Zhang, D.-L., and K. Gao, 1989: Numerical simulation of an intense squall line during 10–11 June 1985 PRE-STORM. Part II. Rear inflow, surface pressure perturbations, and stratiform precipitation. *Mon. Wea. Rev.*, **117,** 2067–2094.

Zipser, E. J., 1988: The evolution of mesoscale convective systems: Evidence from radar and satellite observations. *Tropical Rainfall Measurements,* J. S. Theon and N. Fugano, Eds., Deepak, 159–166.